OPTICAL AND ELECTRONIC PROPERTIES OF HEAVILY DOPED POLYACETYLENE

BY

Xiao-Qing Yang

A DISSERTATION PRESENTED TO THE GRADUATE SCHOOL
OF THE UNIVERSITY OF FLORIDA IN
PARTIAL FULFILLMENT OF THE REQUIREMENTS
FOR THE DEGREE OF DOCTOR OF PHILOSOPHY

UNIVERSITY OF FLORIDA

1986

ACKNOWLEDGMENTS

It is with great pleasure that I thank my adviser, Prof. David Tanner, for his continuous support, guidance, patience and encouragement all throughout my graduate career. I would like to thank my committee, Prof. E.D. Adams, Prof. G. Ihas, Prof .S.B. Trickey and Prof. K.B. Wagener, for their stimulating discussions and suggestions.

I would like to thank Prof. A.J. Epstein for his support and guidance at the Xerox Webster Research Center where I completed part of this study in 1984.

I am grateful to Prof. A. MacDiarmid, Mr. R. Weagley and Ms. G. Arbuckle for preparing polyacetylene samples used in this experiment. I would like to thank Dr. M.J. Rice for his valuable suggestions.

I also want to express my appreciation to my fellow graduate students, staff members of Physics Department shop, and engineers of condensed matter physics group for their technical support and computer software development.

I would like to thank my parents and sister for providing a constant source of support and encouragement. Very special thanks go to my wife, Lan-Feng, whose help and understanding were very important during my studies.

A final thanks is extended to the National Science Foundation for support through the grant NSF-Solid State Chemistry, DMR-8218021, and DMR-8416511.

TABLE OF CONTENTS

page

ACKNOWLEDGMENT.. ii

ABSTRACT.. iv

CHAPTER

I INTRODUCTION.. 1

II BASIC THEORY.. 6

- Molecular Orbitals of Electrons and Conjugated Polymers.......................... 6
- Peierls Instability and Bond Alternation........... 9
- Conjugational Defects and Quasi-Particles.......... 13
- Charge Transport Mechanism and Insulator-Conductor Transition............... 32
- Optical Properties of Doped Polyacetylene.......... 48

III OPTICAL TECHNIQUES.. 86

- The Monochromator.................................. 86
- The Interferometer.................................. 93

VI DATA AND RESULTS.. 105

- Segmented Polyacetylene-$[CHD_y(I_3)_z]_x$............... 105
- Heavily Doped Polyacetylene......................... 119

V DISCUSSION AND CONCLUSIONS.................................. 160

- Segmented Polyacetylene and Soliton................ 160
- Perchlorate Doped Polyacetylene.................... 166

APPENDIX KRAMERS-KRONIG ANALYSIS....................... 171

REFERENCES... 176

BIOGRAPHICAL SKETCH.. 181

Abstract of Dissertation Presented to the Graduate School
of the University of Florida in Partial Fulfillment of the
Requirements for the Degree of Doctor of philosophy

OPTICAL AND ELECTRONIC PROPERTIES OF HEAVILY DOPED POLYACETYLENE

BY

Xiao-Qing Yang

May 1986

Chairman: David Tanner
Major Department: Physics

We undertake a systematic study of the temperature dependent AC and DC conductivity, infrared and optical properties of a conducting polymer, polyacetylene. The samples studied were perchlorate-doped polyacetylene, $[CH(ClO_4)_y]_x$ and a segmented polyacetylene, $[CHD_y]_x$, in which up to 17% of the CH units had been replaced by (sp^3-hybridized) CHD units. The latter samples were prepared by Na-doping of trans-$[CH]_x$ and subsequent compensation by CH_3OD.

At high concentration of perchlorate dopant, polyacetylene undergoes a transformation into a state characterized by high DC conductivity, by a large Pauli susceptibility, and by the absence of the interband transition of the undoped polymer. The infrared and optical spectra show a pseudogap at about 0.2 eV and vibrational modes which imply that the carbon-carbon bond length is not uniform. We conclude that this state is best described as a gapless incommensurate Peierls insulator.

For $[CHD_y]_x$ with y=0.17, the temperature and frequency dependence of the conductivity is much stronger than $[CH]_x$. Upon light doping with iodine, this dependence qualitatively resembles that of ordinary polyacetylene and fits the intersoliton isoenergetic hopping theory of Kivelson. At heavy doping, the DC conductivity is much less, whereas the temperature dependence is stronger than that of ordinary $[CH]_x$ doped to similar level. Optical studies on these segmented polyacetylene samples show the valence-to-conduction band transition in the segmented polymer is shifted to slightly higher frequency and reduced by half in intensity. This phenomenon might be related to a bimodal distribution of conjugation lengths. Treatment with iodine produces strong doping-induced infrared absorption at 880 cm^{-1}, 1400 cm^{-1}, and near midgap. The maximum dopant concentration achieved appeared to be smaller than in ordinary $[CH]_x$, suggesting that only conjugated segments longer than some minimum length can accept dopant.

CHAPTER I
INTRODUCTION

Conducting polymers have attracted a great deal of attention in recent years, due both to possible industrial application of these new material and to fundamental physical concepts which can be studied in these substances[1]. Among all of the newly developed conducting polymers, almost 90% of the research is focused on polyacetylene because of the high conductivity upon doping and its one-dimensional character.

From the materials science point of view, conducting polymers are an attempt to combine the electrical behaviour of metals with the mechanical properties of plastics. Applications in microwave shielding, solar cells, Schottky diodes and high power rechargeable batteries have been discussed. A very exciting suggestion is that they might be used in molecular electronics[2].

From the theoretical physics point of view, conducting polymers provide prototypes for one-dimensional systems. Defects in this system, which disturb the bond conjugation, exhibit many aspect of quasi-particles and often are described as solitons, polarons, or bipolarons, which are concepts developed in relativistic field theory[3]. Since the discovery of the fractional Quantum Hall effect, fractional charge and its ramifications have been widely studied. One-dimensional states with fractional charge found in relativistic field theories have strong similarities to those predicted for quasi-one-dimensional conductors[4].

In condensed-matter physics, conducting polymers provide a quasi-one-dimensional microcosm to investigate energy band structures, electric charge transport properties, electron--electron corelations, electron-phonon interactions, phase transitions, and the relationship among these important physical properties.

To characterize conducting polymers, various modern experimental techniques have been used: electron and X-ray diffraction and magnetic resonance to determine their structure, infrared and optical studies to probe their excitation spectra, DC and AC conductivity measurements to obtain charge transport properties, suceptibility measurements to get magnetic properties, and ESR measurements to investigate the nature (density, mobility, etc.) of unpaired eletron spins.

Since Shirakawa and co-workers first synthesized free standing silvery polyacetylene film[5] in 1974, dozens of new conducting polymers have been synthesized and investigated[6].

The main goal of polymer chemists has been to find new conducting polymers which can be synthesized by the conventional polymer techniques while not losing their conductivity rapidly in the open air (unlike polyacetylene). Significant progress has been made by several research groups[7] but the conductivity of these new conducting polymers is at most only 10% of polyacetylene. As far as for the interesting fundamental physical problems remaining unanswered for conducting polymers, polyacetylene will still be a key element of research in this field. This is why much basic research is still focused on polyacetylene, even though its nonsolubility and instability in the air restricts its application.

The conductivity of polyacetylene can be manipulated over an enormous range of values, from insulator (10^{-12} mho/cm) to good conductor (10^{3} mho/cm), by doping. While the conductivity is increased very rapidly upon light doping, the magnetic spin susceptibility, a Curie-Law contribution, is reduced. The Pauli susceptibility appears only with heavy doping. This result indicates that the charge carrier is spinless[8]. This extraordinary behavior tells us polyacetylene must have a completely different charge transport mechanism from ordinary semiconductors and metals. Intense studies of the charge transport mechanism and insulator-conductor phase transition have led to many different theoretical models. Among them, the soliton model proposed by Rice[9] and Su-Schrieffer-Heeger(SSH)[10], and its continum version by Takayami-LinLiu-Maki(TLM)[11] has been successfully used to describe the ground state and nonlinear excitations of trans-polyacetylene. The intersoliton hopping model of Kivelson[12] and variable range hopping model[13] are in good agreement with experiments for lightly and moderately doped polyacetylene. But the theories for heavily doped polyacetylene are not well established. The controversy has focused on, first, whether heavily doped polyacetylene is a metal or not and, second, the nature of the insulator-conductor phase transition. Kivelson and Heeger[14] claim that heavily doped polyacetylene is a metallic state, and propose a first-order insulator-metal phase transition theory. Dong[15] proposed a Mott transition model emphasizing the important role of the Coulomb interaction and also claims that heavily doped polyacetylene is a metallic state. Many researchers believe that the metallic state is formed by closing the Peierls gap through suppression of the bond-alternation upon heavily doping[16]. In contrast, Rice and Mele[17] have proposed a completely different model. They claim that the heavily-doped polyacetylene is not metallic and that the phase transition is a comensurate-incomensurate charge density wave (CDW) transition. In order to clear up the charge transport and insulator-metal phase transition questions, systematic experimental research program on heavily doped polyacetylene needs to be done. Through coordinated optical, transport and magnetic studies, a comparison between experimental results on heavily doped polyacetylene and these different models will be made in this dissertation.

Another controversal problem is whether charged soliton diffusion or intersoliton hopping is the dominant effect in charge transport for lightly doped polyacetylene. Optical and transport studies on segmented polyacelylene presented in this dissertation will help to understand this problem and provide more information about the distribution of conjugational defects and interchain interactions as well.

Chapter II is a review of the basic theory of charge transport and the insulator-conductor phase transition in polyacetylene. The important experimental results, the predictions of the optical, magnetic and transport properties, and the controversies which arise in the different models will be presented. The most commonly used terminology in this field will also be introduced in this chapter. Chapter III will describe the optical techniques used in this study. Data and its analysis will be presented in chapter IV along with the sample preparation techniques. Discussion and conclusion are presented in chapter V.

CHAPTER II
BASIC THEORY

Molecular Orbitals of Electrons and Conjugated Polymers.

Polyacetyene, the simplest linear chain organic conjugated polymer, has two different "stereoisomers", i. e., the cis- and trans- isomers shown in Fig.2-1. (cis, from the Latin: on this side; trans, from Latin: across; or in other words, hydrogen atoms arranged to be as close as possible from each other in cis; otherwise is in trans.) The trans-$[CH]_x$ is the more stable isomer. Systems with extended π bonds are called conjugated system. In order to understand the term "extended π bond," we need to start from the theory of molecular orbital and covalent bonding.

According to molecular orbital theory, when two atoms are brought together to form a diatomic molecule, the wave functions (orbitals) of the covalent electrons in the molecule will be formed from a linear combination of the atomic wave functions (orbitals) of the constituent atom. This treatment of molecular orbitals is called LCAO, which stands for Linear Combination of

Atomic Orbitals. In the simplest case, there are two newly formed molecular orbitals and two energy levels. The lower level, the ground state, is called the bonding orbital, while the higher one is the antibonding orbital. The bond types are characterized by the angular momentum projection of the molecular orbital along the bonding axis. Greek letters σ, π, δ, ... are used to specify the projection as 0, $h/2\pi$, $2(h/2\pi)$.... respectively; σ^*, π^*.... are the symboles for the antibonding orbitals. The symmetry about the bonding axis is also specified: a σ bond has circular symmetry in cross section taken perpendicular to the bond axis. The π bond has a symmetric mirror plane through the bond axis; this mirror plane is also the nodal plane(nodal plane means that in which the wave function is zero.) Examples of σ and π bonds are shown in Fig.2-2[18].

For some molecules, the molecular energy can be reduced by reforming the atomic orbitals of each atom into new linear combinations before constituting the molecular orbitals. This procedure is called hybridization. Two important hybridized orbitals, sp^2 and sp^3, are shown in Fig.2-3[18].

The "extended π bond" can be easily understood by investigating the benzene ring as shown in Fig.2-4[18]. Three of the four carbon covalent electrons (s,p_x,p_y) form σ bonds with two neighboring carbon atoms and one hydrogen atom through sp^2

hybridization. The remaining electron in a p_z orbital, could form a π bond with either of the two neighboring carbon atoms, thereby making the benzene molecule a single-double bond alternating structure. But theoretical calculation[18] showed that the energy level of a extended π bond formed from the six p_z orbitals is lower than the sumation of three individual π bonds. Experiments[18] showed the bond lengths of all the six bonds in benzene are identical (1.39Å), shorter than the typical single bond length (1.54 Å) but longer than the double bond length(1.34Å). A bond formed from more than two atomic orbitals called an extended π bond. Molecules and polymers with the extended π bond are called conjugated molecules and conjugated polymers.

The structure of polyacetylene could be viewed in this way: breaking a benzene ring, streching it to a linear chain, then repeating many of these to form a long chain. Each carbon atom is bonded with two neighboring carbon atoms and one hydrogen atom through σ bond by sp^2 hybridization. The remaining covalent electrons, a p_z orbital from each carbon atom, interact among themselves to form an extended π bond. As a conjugated polymer, polyacetylene should have an uniform bond length with extended π bond as in Fig.2-5, instead of the single-double bond alternation of Fig.2-1. But due to the so-called "Peierls instability" [19] in one-dimensional systems, the uniform bond length will change into a single-double bond alternation through dimerization.

Peierls Instability and Bond Alternation

Using the language of energy band theory in condensed matter physics, polyacetylene can be described by the tight binding approximation. When free atoms are brought together, the Coulomb interaction between the atom cores and the electrons splits the energy levels, spreading them into bands. So, instead of having $\sigma-\sigma^*$ bond and $\pi-\pi^*$ bond energy levels as in ethene, we have $\sigma-\sigma^*$ energy band and $\pi-\pi^*$ energy band in polyacetylene. There is one electron per primitive cell in polyacelene, so the $\pi-\pi^*$ band is a half filled conduction band. Therefore, polyacetylene should be a conductor. But experiments showed that trans-(cis-) polyacetylene has a semiconducting energy band structure with a 1.4eV (1.9eV) band gap.

The semiconducting state is a result of the Peierls instability of a one-dimensional metal. In simplified form, the Peierls instability can be explained in the following way. The periodic potential in a crystal creates an energy gap at the boundary of the first Brillouin Zone ($k=\pi/a$). If we assume a deformation in the crystal which changes the lattice constant from "a" to "2a", a new energy gap will be formed at $k=\pi/2a$. Normally this deformation does not occur because the elastic energy created by the deformation gives a net increase in the total energy of the system. But in the one-dimenssional system, if the temperature is low enough that the Fermi surface (a plane at $k=k_F$ perpendicular to the chain direction for quasi-one-dimensional system; two points at $k=\pm k_F$ for a one-dimensional system) is sharp, and if $k_F=\pi/2a$, the lattice deformation of period 2a (dimerization in this case) will take place. In this situation, the energy of occupied states is lowered and the energy of empty states raised. So the increase in elastic energy is balanced by a reduction of the electronic energy.

The Peierls transition also can be viewed as a result of the electron-phonon interaction[20]. At low temperature, all the available states for electrons are near the Fermi surface. There is a strong interaction between these electrons and acoustic phonons with wave vector $2k_F$, which can scatter electron from $\pm k_F$ to $\mp k_F$. This causes a softening, or dip in frequency (called a Kohn anomaly), of the $2k_F$ phonons. When the temperature is below T_p, the frequency of $2k_F$ phonons goes to zero; this means that the coresponding vibrational mode becomes time independent, i. e., the lattice distortion of $ma=\pi/k_F$ is "frozen in." Here "a" is the lattice constant and "m" is an integer. For dimerization, m=2. The interesting similarity between the Peierls transition and the superconducting transition will be mentioned many times in this work. Here we point out that they both create an energy gap and form electron pairs through the electron-phonon interaction. The difference is that in the Peierls transition, the pairs are formed by pairing two electrons in a double bond in real space instead of pairing in k-reciprocal space between two electrons at opposite positions on Fermi surface as in BCS theory.

This Peierls transition makes polyacetylene a semiconductor with a 1.4 eV band gap and a single-double bond alternation. Compared to the typical values of 1.54 Å for a single bond and 1.34 Å for a double bond in other organic molecules, the single bond length is found to be about 1.45 Å and the double bond length is 1.39 Å.

Attempts to model polyacetylene as a conventional semiconductor were unsuccessful. For three - dimensional semicondutors, donors or acceptors can be introduced by doping. They will form impurity levels in the band gap and will contribute spin 1/2 charge carriers, i. e., electrons or holes, in the conduction or valence band by thermal or photo excitation. These spin 1/2 charge carriers will increase with increasing dopant concentration and will contribute to a temperature dependent Curie magnetic susceptibility as well as the electric conductivity. When the dopant concentration reaches a critical level, the impurity wave functions will overlap, and the Anderson transition will change the semiconductor into a metal, characterized by a finite density of states at the Fermi level. Further doping above this critical level will increase the temperature independent Pauli susceptibility which is proportional to the density of states. When applying this theory to polyacetylene, several important experimental results could not be interpreted, especially the reversed spin-charge relation. Conductivity and electron spin resonance (ESR) measurements[20] showed that one Curie spin in 3000 CH units is formed during cis-trans isomerization from no-Curie-spins in pure cis-$[CH]_x$. With light doping ($y < 1\%$), these Curie spins decrease almost to zero while the conductivity increases greatly. Further doping (up to 5%) causes a rapid increase of the conductivity but the number of Curie spins remains almost zero. These results indicate that the charge carriers in doped polyacetylene are spinless instead of the spin 1/2 electrons or holes of a conventional semiconductor. This anomalous phenomenon is called the reversed spin-charge relation. Most of the models introduced to explain this relation concentrate on various conjugational defects which are described by the terminology of relativistic quantum field theory as quasi-particles: solitons, polarons and bipolarons. Among these models, the topological soliton theory proposed by M.J. Rice[9] and Su, Schrieffer, and Heeger (SSH)[10] is the first and most successful model.

Conjugational Defects and Quasi-Particles

Topological Soliton and SSH Model

A water wave soliton was first described in the 19th century by John Scott Russell, a British engineer, who saw a wave roll for miles along a narrow canal with no apparent change. (In this case, the soliton was a real wave that separated two regions of placid water). The soliton is characterized by the kinematic behavior: it does not change its shape while it is moving. In contrast a wave packet often disperses because it is a linear combination of harmonic components which get out of phase as they propagate.

Trans-$[CH]_x$ dimerized through the Peierls transition has two degenerate ground states: phase A and phase B as shown in Fig 2-6. An order parameter(a term used in Landau-Ginzberg mean field theory) u_n is defined as a lattice distortion with respect to the undimerized position at site n. Joining phase A and phase B creates a conjugational defect at the joint site which causes a "kink" of u_n at this site, called a "topological soliton."

The soliton state is not simply localized at one atom site, since the elastic energy would prefer to spread this defect through the whole chain, but the Peierls distortion would favor a narrow kink. The competition between these two effects make the soliton spread over about 15 CH units.

As we know from the superconductive (or superfluid) state, breaking the electron pair creates a quasi-particle; breaking the electron pair at a double bond in trans-$[CH]_x$ creates a soliton. The name comes from the ϕ^4 equation of quantum field theory which has the soliton solution for the "kink" state. Similarly, all other conjugational defects can be described as quasi-particles created by breaking electron pairs at a double bond. And, they all obey the law of particle conservation: if not present on the polymer chain from the chemical synthesis, they can only be created as particle and anti-particle pairs. A soliton-antisoliton pair is shown in Fig.2-7.

The unpaired electrons at neutral soliton states have spin 1/2; the positively and negatively charged solitons are spinless. The spin-charge reversal could be perfectly explained by this soliton model. The neutral solitons created during cis-trans isomerization are free spins in undoped trans-$[CH]_x$. The number of free spins decreases upon very light doping because the ionized soliton carries no spin. Further doping creates more spinless charged soliton-antisoliton pairs.

The electronic level localized at a "kink" site has an energy level ω_s at the center of the Peierls gap because of symmetry. The energy level of a soliton can be explained in the following way. Consider a neutral chain of 2n+1 [CH] units. Joining the two ends to form a ring will give 2n+1 bonds in total. There must be at least one soliton defect somewhere along the chain. So for any Hamiltonian that has charge conjugation symmetry (i. e., for every electronic level at E there is a level at energy -E), there is a level exacty at midgap associated with the kink. The chain with even number [CH] units can be explained by the same manner with an even number of kinks. The 2n electrons in the valence band are paired and have no spin. The soliton state can be unoccupied (positively charged, spinless), singly occupied (neutral, spin 1/2), or doubly occupied (negatively charged, spinless).

Starting from a Huckel-type Hamiltonian for polyacetylene Su, Schrieffer, and Heeger[10] calculated the ground state energy and the energy gap due to the Peierls distortion. By using a trial function and numerical method, they also calculated the formation energy, activation energy for motion, length and effective mass of the soliton in polyacetylene with good agreement with experiment. The basic assumptions for a Huckel-type Hamiltonian are as follows:

1. Only the π-electrons are explicitly considered. The effect of σ-electrons are contained in the parameters of the theory such as the elastic constant.
2. The π-electron states are calculated with respect to fixed nuclear configuration (Born-Oppenheimer approximation).
3. The many-body Hamiltonian (including electron-ion and electron-electron interaction) is replaced by a sum of single-particle terms leading to an effective Hamiltonian H_{eff}.
4. The eigenfunctions of H_{eff} are taken as linear combinations of atomic orbitals $|n\rangle = (r-R_n)$ where R_n is the position vector of the nth C atom. The overlap matrix elements are limited to the nearest neighbors, that is, $\langle n|m\rangle=0$ if $n=m$ and $\langle n|H_{eff}|m\rangle=0$ except for $n=m$, $n=m+1$, and $n=m-1$ (the tight-binding approximation).

The SSH Hamiltonian is expressed as a function of the order parameter u_n:

$$H= -\sum_{n,s} t_{n+1,n} \left(C^{+}_{n+1,s}C_{n,s} + C^{+}_{n,s}C_{n+1,s}\right) + \frac{1}{2}\sum_{n} K_{o}(u_{n+1} - u_{n})^{2} + + \frac{1}{2}\sum_{n} M\dot{u}^{2} \tag{2-1}$$

where $C^{+}_{n,s}$ and $C_{n,s}$ create and destroy electrons of spin s(1/2) on the nth CH unit, $t_{n+1,n}$ is the hopping integral, "K" is the effective bond spring constant, and M is the total mass of the CH unit. The first term is the contribution of one-dimensional electrons, the second term is the elastic energy of σ bonds expanded about the undimerized state to second order (since $u_{n+1}-u_n$ is small), and the last term is the kinetic energy of nuclear motion. The hopping integral $t_{n+1,n}$ depends on the bond length and can be expanded in powers of u_n up to the quadratic term. For simplicity the quadratic term can be absorbed in the modified spring constant K. Then we have

$$t_{n+1,n} = t_o - \alpha(u_{n+1} - u_n) \tag{2-2}$$

where α is electron-phonon coupling constant and t_o depends on the π-bandwidth ($W=4t_o$ is commonly used). So, for a perfect dimerized chain, i. e., $u_n=(-1)^n u$, the first two terms of Eq.2-1 become

$$H^{dim}(u) = -\sum_{n,s} [t_o+(-1)^n 2\alpha u]\,(C^{+}_{n+1,s}C_{n,s} + C^{+}_{n,s}C_{n+1,s}) + 2NKu^2 \tag{2-3}$$

Using the well known result of the tight-binding approximation for one-dimensional systems, the zero-order(u=0) eigenenergy and eigenstates for conduction and valence bands are

$$E^{ov}(k)=-2t_o\cos(ka)=-\varepsilon_k \tag{2-4a}$$

$$E^{oc}(k)=2t_o\cos(ka)=\varepsilon_k \tag{2-4b}$$

$$\Psi^{v}=N^{-1/2}\sum_n e^{ikan}\,\Phi_n \tag{2-5a}$$

$$\Psi^{c}=N^{-1/2}\sum_n e^{ikan}(-1)^n\,\Phi_n \tag{2-5b}$$

Here Φ_n is the π orbital on the nth unit. Define operators in k space:

$$C^{v}(k,s)=N^{-1/2}\sum_n e^{ikan}C_{ns} \tag{2-6a}$$

$$C^{c}(k,s)=N^{-1/2}\sum_n e^{ikan}(-1)^n C_{ns} \tag{2-6b}$$

The perfect dimerized Hamiltonian in k representation is

$$H^{dim}=\sum_{k,s}[\varepsilon_k(C^{c+}_{ks}\,C^{c}_{ks}-C^{v+}_{ks}\,C^{v}_{ks})+4\alpha u.\sin(ka).(C^{c+}_{ks}\,C^{v}_{ks}+C^{v+}_{ks}\,C^{c}_{ks})]+ \\ +2NKu^2 \tag{2-7}$$

It can be diagonalized into

$$H^{dim} = \sum_{ks} E_k(n^c_{ks} - n^v_{ks}) + 2NKu^2 \tag{2-8}$$

where $n^c_{ks} = a^{c+}_{ks} a^c_{ks}$ and $n^v_{ks} = a^{v+}_{ks} a^v_{ks}$ is the occupation number operator for conduction and valence band respectively with the definition of a^c_{ks} and a^v_{ks} as

$$a^v_{ks} = a_k C^v_{ks} + b_k C^c_{ks} \tag{2-9a}$$

$$a^c_{ks} = a^*_k C^c_{ks} - b_k C^v_{ks} \tag{2-9b}$$

and

$$|a_k|^2 + |b_k|^2 = 1 \tag{2-10}$$

The eigenenergy E_k in Eq.2-8 is

$$E_k = (\varepsilon^2_k + \Delta^2_k)^{1/2} = [(2t_o \cdot \cos(ka))^2 + (4\alpha u . \sin(ka))^2]^{1/2} \tag{2-11}$$

and the gap parameter Δ_k is defined by

$$\Delta_k = 4\alpha u.\sin(ka) \tag{2-12}$$

From the spectrum Eq.2-11, we get $E_k = \pm 4\alpha u$ for $k = k_F = \pi/2a$, i. e., the Peierls gap $2\Delta = 8\alpha u$. The ground state energy as a function of u can be derived from Eq.2-8 with the condition $n^v_{ks} = 1$ and $n^c_{ks} = 0$:

$$\begin{aligned} E_o(u) &= -2 \sum_k E_k + 2NKu^2 \\ &= -2 \sum_k [(2t_o.\cos(ka))^2 + (4\alpha u.\sin(ka))^2\ ]^{1/2} + 2NKu^2 \end{aligned} \tag{2-13}$$

Replacing the sum by an integral within the first Brillouin zone, we get

$$\begin{aligned} E_o(u) &= \frac{-2L}{\pi} \int_o^{\pi/2a} [(2t_o.\cos(ka))^2 + (4\alpha u.\sin(ka))^2]^{1/2} dk + 2NKu^2 \\ &= -\frac{4Nt_o}{\pi} E(1-Z^2) + \frac{NKt_o^2\ Z^2}{2\ \alpha^2} \end{aligned} \tag{2-14}$$

where $E(1-Z^2)$ is the elliptic integral,

$$Z = t_1/t_o = 2\alpha u/t_o \tag{2-15}$$

For small Z

$$E(1-Z^2) \simeq 1 + \frac{1}{2}(\ln 4/|Z| - \frac{1}{2})Z^2 + \ldots \qquad (2\text{-}16)$$

Using $K=21\text{eV}/\text{Å}^2$, the π bandwith as $W=4t_o=10\text{eV}$, and choosing α so that $E_o(u)$ has a minimum when $E_g=4t_1=8\alpha u=1.4\text{eV}$, $E_o(u)$ is shown in Fig.2-8. With this choice of parameters, the calculated α is 4.1eV/Å. The double well potential in Fig.2-8 has two minima at $u=\pm u_o$ with $u_o=0.04$Å. The bond-length change is +0.046Å. So the Peierls dimerization can be explained quantitatively within the SSH model with degenerate ground state phases $A(u=u_o)$ and phase $B(u=-u_o)$.

The double well potential in Fig.2-8 is topologically equivalent to the ϕ^4 mode[21,22] (see Fig.2-9). So the order parameter pattern $u_n=u_o.\tanh(na/\xi)$ which is well known in type II supperconductors was choosen as the ansatz. Using a Green's function method and numerical calculations, a soliton formation energy $E(d)$ as a function of the soliton half width length $d=\xi/a$ is shown in Fig.2-10[10]. Choosing $E_g=1.4\text{eV}$, $d=7$ and $E_s=0.42\text{eV}$ is obtained. The effective mass of soliton M_s can be calculated from the kinetic energy of a moving domain wall:

$$u_n(t)=u_o.\tanh[(na-v_s t)/d.a] \qquad (2\text{-}17)$$

The kinetic energy is

$$\frac{1}{2} M_s v_s^2 = \frac{1}{2} M \sum_n (\dot{u}_n)^2 = \frac{1}{2} M v_s^2 \frac{u_o^2}{d^2 a^2} \sum_n \operatorname{sech}^4[\frac{n}{d}] \qquad (2\text{-}18)$$

Then we get $M_s = 4u_o^2 M/3da^2 \approx 6m_e$, the last equality is obtained by using a suitable value of u_o and d for E_g=1.4eV. This small mass indicates a high mobility for the soliton. Since the characteristic length for a fluctuation, the soliton length ξ, is much bigger than the lattice constant "a", a continuum limit from the SSH Hamiltonian should be a good approximation. The continuum version was carried out by Takayama, Lin-Liu and Maki[11] (TLM model).

TLM Model

The TLM model has an analytic solution for the dimerized ground state, as well as for the soliton, polaron and bipolaron excitations. The soliton length was found to be $\xi_o = \hbar v_F/\Delta_o = 2t_o/\Delta_o$, where v_F is the Fermi velocity. (From now on, we will choose units such that $\hbar$=1), The formation energy $E_s = 2\Delta_o/\pi$ was also calculated analytically. To obtain the TLM model, one expands the electronic operator C_{ns} in the field operators $u_s(x)$ and $v_s(x)$ representing particles close to k_F and $-k_F$:

$$C_{ns} = a^{-1/2}[u_s(x)\, e^{ik_F na} - iv_s(x)\, e^{-ik_F na}] \qquad (2\text{-}19)$$

Similarly, one writes u_n in terms of the gap parameter $\Delta(x)$ as

$$u_n = \frac{1}{4\,\alpha}\, [\Delta^+(x) e^{2ik_F na} + \Delta(x) e^{-2ik_F na}] \qquad (2\text{-}20)$$

and linearizes the electron dispersion around $k_F = \pi/2a$:

$$\varepsilon\,(k) = -2t_o \cos[(k+k_F)a] = \pm 2t_o \sin(ka) \;\simeq\; \pm 2t_o . a . k \equiv \pm v_F . k \qquad (2\text{-}21)$$

Then, the SSH Hamiltonian becomes

$$H = \frac{K}{8\alpha^2\, a} \int dx\, \Delta^2(x) + \sum_s \int dx\, [-iv_F[u_s^+(x) \frac{\partial}{\partial x} u_s(x) -$$

$$-v_s^+(x) \frac{\partial}{\partial x} v_s(x)] + \Delta(x)[u_s^+(x) v_s(x) - v_s^+(x) u_s(x)] \qquad (2\text{-}22)$$

Defining

$$\Psi(X) = \begin{bmatrix} u(x) \\ v(x) \end{bmatrix} ; \qquad \Omega_Q^2 = \frac{4k}{M} ; \qquad g = 4\alpha \left(\frac{a}{M}\right)^{1/2}$$

Eq.2-22 becomes the TLM Hamiltonian:

$$H = \frac{\Omega_Q^2}{2g^2} \int dx\, \Delta^2(x) + \int dx \Psi^+(x) [-iv_F\, \sigma_3 \frac{\partial}{\partial x} + \Delta(x)\sigma_1]\, \Psi(x) \qquad (2\text{-}23)$$

where σ_i is the ith Pauli matrix. Varying Eq.3-23 with respect to $u^*(x)$ and $v^*(x)$ gives

$$-iv_F \frac{\partial u(x)}{\partial x} + \Delta(x).v(x) = E_n u(x) \qquad (2\text{-}24a)$$

$$iv_F \frac{\partial v(x)}{\partial x} + \Delta(x).u(x) = E_n v(x) \qquad (2\text{-}24b)$$

Varying Eq.2-23 with respect to $\Delta^+(x)$ gives the self consistency equation

$$\Delta(x) = - \frac{g^2}{\Omega_Q^2} \sum_{\nu,s}{}' [u_\nu^*(x)\, v_\nu(x) + v_\nu^*(x)\, u_\nu(x)] \qquad (2\text{-}25)$$

where the sum is over spin components and occupied electron levels. These equations are known from the theory of inhomogeneous superconductors as the Bogoliubov-Gennes equations[23]. Differentiating Eq.2-24 with respect to x and introducing

$$f_+(x) = u(x) + iv(x) \qquad f_-(x) = u(x) - iv(x) \qquad (2\text{-}26)$$

Eq.2-24 becomes

$$[v_F \frac{2\partial^2}{\partial x^2} + E_n^2 \pm v_F \frac{\partial\Delta(x)}{\partial x} - \Delta^2(x)]\, f_{-}^{+}(x) = 0 \qquad (2\text{-}27)$$

This is a "Schrodinger-like" equation.

For the homogeneous dimerized lattice: $\Delta(x)=\Delta_o$, the solutions are plane wave function with the energy dispersion relation:

$$E^2(k) = \omega^2 = \Delta_o^2 + v_F^2\, k^2 \qquad (2\text{-}28)$$

and the energy gap is obtained from the self-consistency equation

$$2\Delta_o = 2W\, e^{-1/2\lambda} \qquad (2\text{-}29)$$

where $W=4t_o$ is the π band width and

$$\lambda = \frac{2\,\alpha^2}{\pi t_o K} = \frac{g^2}{\pi\Omega_Q^2\, v_F} \qquad (2\text{-}30)$$

For the inhomogeneous state, using the ansatz

$$\Delta(x) = \Delta_o \tanh(x/\xi_s) \qquad (2\text{-}31)$$

Eq.2-27 is explicitly solved in terms of hypergeometric function [24]. It is quite amazing that the self-consistency condition Eq.2-25 is identically satisfied, proving that Eq.2-31 is an exact solution. The soliton formation energy, defined as the difference between the mean field (MF) energies in presence of a soliton and the soliton free ground state [11], is

$$E_s=2\Delta_o/\pi \tag{2-32}$$

in good agreement with the numerical result of SSH model ($E_s=0.6\Delta_o$).

Polaron Solution

Another exact solution which can be derived from the TLM model is the polaron (equivalent to bags in field theories). A polaron is formed by the self trapping of an added electron or hole into the dimerized lattice. It is topologically equivalent to a bound pair of a neutral soliton and charged antisoliton. (or charged soliton and neutral antisoliton). The order parameter ansatz for a polaron is

$$\Delta_p(x)=\Delta_o - k_o v_F\ [\tanh k_o(x+x_o) - \tanh k_o(x-x_o)] \tag{2-33}$$

with

$$\tanh(2k_o x_o) = k_o v_F / \Delta_o \qquad (2\text{-}34)$$

The extended conduction and valence band electron wave function derived from Eq.2-24 are basically the same as in the defect-free dimerized chain with a phase shift due to the defect. But two localized states are formed symmetrically in the gap at $\varepsilon_{-}^{+} = \omega_{o-}^{\ +}$ with the dispersion relation:

$$\omega_o^2 = \Delta_o^2 - k_o^2 v_F^2 \qquad (2\text{-}35)$$

It is very interesting to note that Eq.2-33 satisfies Eq.2-24 for all ω_o. But only for certain values of ω_o can the self-consistent equation 2-25 be satisfied: $\omega_o=\Delta_o$ corresponds to uniform dimerization; $\omega_o= 0$ corresponds to an infinitely separated soliton-antisoliton pair; $\omega_o= 2^{-1/2}\Delta_o$ corresponds to a polaron. So, all of these quasi-particles can be treated in a unified theory.

Eq.2-24 is exactly equivalent to the static version of the semiclassical equation of the N=2 Gross-Neveu model field theory [25-27]. As shown by Dashen et al. in reference 28, for general N there exist bag-like self-consistent solutions in which all negative energy states, including the bound state with $E=-\omega_o$, are occupied by N fermions and the positive energy bound state is occupied by n fermions. By the charge conjugation symmetry of Eq.2-24, there exist an antiparticle (the "hole" polaron) in which the negative energy bound state is occupied by only $N_1 < N$ fermions. The value of ω_o for which the self-consistent equation is satisfied[28] is given by

$$\omega_o(n) = m \cos[\theta(n)] \qquad (2\text{-}36)$$

where $m=\Delta_o$ for polyacetylene and

$$\theta(n) = (n/N) (\pi/2) \qquad (2\text{-}37)$$

The formation energy of the corresponding bag-like excitation is

$$E(n)=(2/\pi) N m \sin(\theta) \qquad (2\text{-}38)$$

using Eq.2-36, Eq.2-37 and Eq.2-38, with $m=\Delta_o$ and N=2, $\omega_o=\Delta_o$, $\omega_o=2^{-1/2}\Delta_o$ and $\omega_o=0$ can be derived for n=0, n=1 and n=2 respectively.

It is more convenient to use the equations developed for trans-$[CH]_x$ equivalent to Eq.2-36 and Eq.2-37. Introducing θ such that

$$k_o\, v_F = \Delta_o \sin(\theta) \tag{2-39}$$

$$\omega_o = \Delta_o \cos(\theta) \tag{2-40}$$

and

$$\theta = (n_+ - n_- + 2)(\pi/4) \tag{2-41}$$

where n_+, n_-=0, 1, 2 is the occupation number of the E_+ and E_- state, respectively. The possible configurations for (n_+,n_-) are (0,0); (0,1); (0,2); (1,1); (1,2); (2,2). n_+=0, n_-=1 corresponds to a hole polaron and n_+=1, n_-=2 corresponds to an electron polaron. From Eq.2-39, Eq.2-40 and Eq.2-41 we get

$$\xi_p = k_o^{-1} = 2^{1/2} v_F \;/\; \Delta_o = 2^{1/2}\, \xi_s \tag{2-42}$$

From Eq.2-38,

$$E_p = E(2) = 2.2^{1/2}\, \Delta_o/\pi \tag{2-43}$$

so the energy level ω_o, formation energy E_p and decay length ξ_p of the polaron are calculated. For $n_+=0$ and $n_-=2$, we get $k_o v_F=0$ and $\omega_o=\Delta_o$. This corresponds to a perfect dimerized ground state; it means a neutral polaron with empty E_+ state will collapse to the vacuum.

Bipolaron Solution

For $n_+=n_-=0$; 1; 2, $k_o v_F=\Delta_o$ and $\omega_o=0$. From Eq.2-34, we get $x_o=\infty$. This means the doubly positively charged, neutral and doubly negatively charged bipolarons are unstable towards infinitely separated soliton-antisoliton pairs. But this result depends on the assumption of equilibrium conditions and infinite long chains. When the end effect becomes important in short chain $[CH]_x$, or high concentration of dopant makes the interaction between defects no longer negligible, the confinement energy might bind a soliton and an antisoliton to form the doubly charged pair defect, i.e., bipolaron. A bipolaron can be viewed either as a doubly charged conjugational defect which is formed from further ionization of a singly charged polaron, or as paired soliton and antisoliton with the same sign of charge (in trans-$[CH]_x$) or paired polarons (in cis-$[CH]_x$). Here we see the bisoliton and bipolaron are the same in trans-$[CH]_x$. When the soliton and antisoliton form a bound pair, the interaction between them will split the $\omega_s=0$ energy level to $\omega_{Bp}=\pm\omega_o$ where $0 < \omega_o < 2^{-1/2}\Delta_o$. The topological feature of the soliton, polaron and bipolaron in trans-$[CH]_x$ are sketched in Fig.2-11. The order parameter, wave function, and energy levels of soliton and polaron are shown in Fig.2-12[25].

In many conducting polymers, such as poly(p-phenylene) (PPP), polypyrrole (PPR), the nondegenerate ground states do not support free solitons. But they show very similar experimental results to trans-$[CH]_x$ (high conductivity, reversed charge-spin relation, and infrared absorption below band edge). In these conducting polymers, polarons and bipolarons may play important roles. The nondegeneracy of the ground state in these polymers leads to a symmetry-broken double well energy curve as shown in Fig.2-13. In this case, a soliton-antisoliton pair separated by a distance "d" would cost energy $d(\delta E/L)$, where $\delta E/L$ is the energy difference per bond between the stable and metastable phases. The doubly-charged bipolaron is energetically prefered over the isolated singly-charged polaron but has a larger size ($2x_o$) than each singly occupied polaron [25].

Most of the equations for trans-$[CH]_x$ in this section can be applied to the nondegenerate case (eg., cis-$[CH]_x$) with small modification. A modified gap parameter $\Delta_m(x)=\Delta_i(x)+\Delta_e(x)$ is used to replace $\Delta(x)$, where Δ_i is the intrinsic gap which is sensitive to electron-phonon coupling, and Δ_e is an extrinsic gap which is a constant. The equation which determines the eigenvalue ω_o for cis-$[CH]_x$ (equivalent to Eq.2-41 for trans-$[CH]_x$) is

$$\gamma \tan\theta = (\pi/4)(n_+ - n_- + 2) - \theta \qquad (2\text{-}44)$$

where $\gamma = \Delta_e / \lambda\Delta_{mo}$ with λ defined in Eq.2-30. For $\gamma=0$, Eq.2-44 becomes Eq.2-41 as expected for trans-$[CH]_x$. From Eq.2-44, we see $\theta < \pi/2$ for any configuration of (n_+, n_-) if $\gamma > 0$, so $k_o v_F < \Delta_{mo}$ and no free soliton-antisoliton pairs is stable in cis-$[CH]_x$.

Starting from the TLM model and using the Gross-Neveu model field theory, all of the conjugational defects can be treated in an unified theory as excited quasi-particles, such as soliton, polaron, and bipolaron. The important physical feature of these quasi-particles are summarized in Table 2-1.

Charge Transport Mechanism and Insulator-conductor Transition

The charge transport properties are the most interesting and controversal topics in polyacetylene. It is hard to imagine that the range of 10^{16} in conductivity could be explained by one transport mechanism. In fact, several mechanisms have been proposed. Among them, the metallic islands model, the amorphous semiconductor model, and the quasi-particle charge transport model are the most interesting models. these models along with the different models of the insulator-conductor transition will be discussed throughout this section.

Metallic Islands Model

In this model it is believed that the aggregation of the dopant causes the formation of grains with metallic-like high conductivity embedded in a semiconducting host material. The insulator-metal transition occurs through a percolation transition in which the metallic grains first become interconnected. Using Maxwell-Garnett theory and effective medium theory, this model predicts a quadratic frequency dependence for the AC conductivity which has been a common feature of composite systems. At low metal concentrations, the temperature dependence of DC conductivity is governed by the semiconducting host and has the form $\sigma \propto \exp(-AT^{-1/2})$ for conductivity. Although some experimental results can be explained by this model, it fails to explain the reversed spin-charge relation. In addition, the quadratic frequency dependence of the AC conductivity has not been observed. So most scientists believe that although the dopant distribution may be nonuniform, it is not segregated into metallic islands for doped polyacetylene.

Amorphous Semiconductor Model

According to x-ray diffraction studies[29], the coherence length for undoped polyacetylene is only 100 Å and decreases to 20 Å upon doping. This indicates that polyacetylene is a highly disordered system. Applying the well-developed theory for the conductivity of amorphous semiconductors on this system would be reasonable.

The temperature and frequency dependence of the conductivity is quite different if the conduction occurs by motion of charge carriers in extended states or by hopping among localized states near the Fermi level. When carriers are excited across the mobility edges into the range of extended states, the conductivity does not depend on frequency, at least in the frequency range up to 10^8 Hz. On the other hand, when conduction occurs by phonon-assisted hopping between localized states, the conductivity increases with frequency. Physically, this is due to the presence of pairs or large clusters of anomalously nearby sites between which electrons can hop at a rate greater than the rate which characterizes the difficult hops necessary to traverse the whole sample for DC conductivity.

When charge carriers are excited across the mobility edge into the range of extended states, the DC conductivity is characterized by a term $\propto \exp[-E_a/kT]$, which is due to the occupation distribution of the excited states. The conductivity for any semiconductor can be expressed in the form

$$\sigma = -e \int N(E)\ \mu(E) k_B T \frac{\partial f(E)}{\partial E}\, dE \qquad (2\text{-}45)$$

where N(E) is the density of states, $\mu(E)$ is the mobility and f(E) is the Fermi-Dirac distribution function.

$$f(E) = \frac{1}{1 + \exp[(E-E_F)/k_B T]} \qquad (2\text{-}46)$$

Using the relationship

$$\frac{\partial f(E)}{\partial E} = -f(E)[1-f(E)]/k_B T \qquad (2\text{-}47)$$

σ can be written as

$$\sigma = e \int N(E)\ \mu(E)\ f(E)[1-f(E)]dE \qquad (2\text{-}48)$$

According to Davis and Mott[30], the Fermi level is situated near the middle of the gap and sufficiently far from E_c(the energy which seperates the extended states from the localized states) that Boltzman statistics can be used for f(E). In the non-degenerate case and under the assumption of a constant density of states and constant mobility, the conductivity is given by

$$\sigma = eN(E_c)kT\ \mu_c \exp[-(E_c - E_F)/kT] \tag{2-49}$$

where μ_c is the average mobility.

Using the Einstein relatation

$$\mu = eD/kT \tag{2-50}$$

where D is the defusion coefficient, Eq.2-49 can be written as

$$\sigma = C_o \exp\ [-E_a / k_B T] \tag{2-51}$$

where C_o is independent of temperature.

When conduction occurs by phonon-assisted hopping between localized states, the temperature dependence of the hopping conductivity near E_F has been given by Mott[31]. When an electron is scattered by phonons from one localized state to another with the energy difference W between the two states, the probability P of this hopping is determined by three factors: (1) The probability of finding a phonon with an excitation energy equal to W, given by $P_W=\exp(-W/kT)$; (2) An attempt frequency f_{ph} which can not be greater than the maximum phonon frequency; and (3) The probability of electron transfer from one state to another. This factor depends on the overlapping of the wave functions. It is given by $P_R=\exp(-2\alpha R)$. Here R is the jumping distance which at high temperature equals the interatomic spacing, and α is a quantity which is representative for the rate of decaying of the wave function at a site. The probability P that an electron jumps will then be expressed by

$$P = f_{ph}\exp(-2\alpha R - W/k_BT) \tag{2-52}$$

Using the Einstein relation $\mu=eD/kT$ and according to the thoery of Brownian motion, the diffusion coefficient is given by

$$D = (1/6)PR^2 \tag{2-53}$$

From Eq.2-52, Eq.2-53, and Eq.2-49,

$$\sigma = (1/6)e^2 R^2 f_{ph} N(E_F).\exp(-2\alpha R) \exp(-W/k_B T) \tag{2-54}$$

As the temperature is lowered, the number and energy of phonons decreases, and the more energetic phonon-assisted hops will progressively become less favorable. Carriers will tend to hop to larger distances in order to find sites which lie closer in energy than the nearest neighbors. This mechanism is the so-called variable range hopping. The most probable hopping distance R no longer equals the interatomic spacing but instead is determined by an optimization procedure used by Mott[31]. If N(W) is the density of states per unit volume per unit energy, then the number of states with energy difference W within a distance R from a particular atom is given by $(4\pi/3)R^3 N(W)W$. The carrier can leave its site only if the number of accessible sites is at least one. So the average energy spacing between states near the Fermi level is

$$W = [(4\pi/3)R^3 N(E_F)]^{-1} \tag{2-55}$$

and the jump probability

$$P = f_{ph} \exp [-2\alpha R - [(4\pi/3) N(E_F)R^3 k_B T]^{-1}] \tag{2-56}$$

The most probable jump distance is found by minimizing the exponent of Eq.2-56

$$R = [(8\pi/9)\alpha\ N(E_F)k_BT]^{-1/4} \tag{2-57}$$

This gives a jump probability of the form

$$P = f_{ph}\ \exp[-2.1[\alpha^3/k_BTN(E_F)]^{1/4}] \tag{2-58}$$

and the conductivity

$$\sigma = \sigma_o(T)\ \exp\ (-2.1[\alpha^3/k_BTN(E_F)]^{1/4}) \tag{2-59}$$

The frequency dependence of the conductivity for variable range hopping has also been derived by Austin and Mott[32]

$$\sigma(\omega) = \frac{\pi}{3}\ e^2k_BT[N(E_F)]^2\ \alpha^{-5}\ \omega[\ln(F_{ph}/\omega\ )]^4 \tag{2-60}$$

Two important features should be noticed from Eq.2-60: (1) $\sigma(\omega)$ varies linearly with temperature. (2) Because of the presence of the logarithmic term $[\ln(F_{ph}/\omega)]^4$, the slope of a plot of ln $\sigma(\omega)$

vs. $\ln(\omega)$ is not a constant, but decreases slightly with increasing frequency of the applied field. Eq.2-60 can be approximated as

$$\sigma(\omega) \simeq \text{Const} \, . \, \omega^{s} \tag{2-61}$$

where s is defined as $d(\ln\sigma)/d(\ln\omega)$ and is given by

$$s = 1 - 4[\ln(f_{ph}/\omega)]^{-1} \tag{2-62}$$

Taking $f_{ph}=10^{13}$ sec^{-1}, the exponent decreases from a value $s=0.84$ at $\omega=10^{2}$ sec^{-1} to $s=0.65$ at $\omega=10^{8}$ sec^{-1}.

Although the reverse spin-charge relation cannot be explained by simply applying the hopping theory for amorphous semiconductors to polyacetylene, the modified hopping theory, i. e., isoenergetic phonon assisted hopping among solitons done by Kivelson[12,33] and variable-range hopping among fixed defect sites(including solitons) done by Kivelson and Epstein[33] are some of the successful models.

Charge Transport Through Quasi-particles.

The only successful model for the reversed spin-charge relation is the soliton model. Photoinduced spectroscopy[34] provided new evidence for this model. Although that it has been widely accepted by scientific community that charge is stored in the form of spinless charged solitons, but how that charge contributes to conductivity is not yet clear. Charged soliton diffusion and hopping among solitons or soliton-like states are two competing models.

According to the intersoliton hopping model of Kivelson [12,35], charged solitons are bound to charged impurity sites by the Coulomb force . The excess charge on the soliton site may make a phonon-assisted hop to a neutral soliton on another chain. If this neutral soliton is near another charged impurity, the energy of the charged carrier before and after the hop is unchanged. This is so called isoenergetic hopping. The temperature dependence of the conductivity is determined by the probability, $\gamma(T)$, that the neutral soliton is near the charged impurity and the initial and final energies are within k_BT each other. The function $\gamma(T)$ is assumed to be proportional to a power law in temperature, T^{n+1}. The spatial dependence of the hopping rate is determined by the wavefunction overlap which is assumed to vary exponentially. The DC conductivity is

$$\sigma_{DC} = Ae^2[\gamma(T)/k_BTN](\xi/R_o^2)y_n y_{ch}(y_n+y_{ch})^{-2}\exp[-2BR_o/\xi] \qquad (2\text{-}63)$$

where A=0.45, B=1.39 are constants determined by experiments, y_n and y_{ch} are the concentrations of neutral and charged solitons per carbon atom respectively, R_o is the typical separations between impurities, and ξ is the average decay length for a soliton.

Mobile neutral solitons play an important role in the Kivelson model. Without mobile neutral solitons, the isoenergetic hopping rate would be too low to have any significant effect.

Based on temperature and frequency dependent conductivity measurements, Epstein[33] showed that the conductivity of undoped and lightly doped (less than 0.01 I_3) trans-polyacetylene is in good agreement with the isoenergetic intersoliton electron hopping model. For intermediate (0.01-0.05 I_3) doping levels, the conductivity is in better agreement with variable range hopping among pinned solitons for trans-polyacetylene [36]. The major problem of variable range hopping models is that the calculated conductivity using the density of states at the Fermi level obtained from magnetic measurements is too low as compared with experiments (several orders of magnitude lower). Epstein pointed out that since the variable range hopping includes states beyond the range of kT from the Fermi level, we cannot simply using the density of states at the Fermi level. Assuming the density of states has a form of $N(\varepsilon)\propto\varepsilon^2$ due to the disorder effect, a good agreement with experimental results was obtained(ε is the energy level measured from Fermi level).

Using the results from in situ doping and ESR measurement, Chung et al.[37] argued against the hopping model for charge transport on the basis of a very low density of states at the Fermi level. So, they insist that charge transport is through charged soliton diffusion. But they added a note at the end of reference 37 saying their result is not necessarily inconsistent with the variable range hopping model if the density of states is no longer a constant near the Fermi level.

Models for the insulator-conductor transition.

One of the early model was the metallic island model. It views the transition as a percolation transition which occurs when the metallic regions first become interconnected. But strong evidence from optical, magnetic and transport experiments ruled out this model. The Anderson transition model for conventional semiconductors was also ruled out because the reversed spin-charge relation for doped trans-polyacetylene cannot be explained. Four competing models and the comparison between their prediction and our experimental result will be discussed through this dissertation.

The "Peierls Gap Closing Model" views the transition as a gap closing process. This model assumes the single-double bond alternation will be suppressed by doping to a critical level. So the Peierls gap created by dimerization will be closed. The π-π^* band will become a nearly half-filled conduction band as in simple metals.

The "Soliton Glass to Soliton Liquid Model" by Dong [15] emphasizes the quasi-particle feature of the soliton. It treated the doped polyacetylene as an ensemble of interacting spinless fermions in an external field produced by the impurity ions. At some critical concentration of dopent, the "soliton glass" will "melt" to "soliton liquid". The transition is caused by screening and correlation effects due to the soliton-soliton and the soliton-ion interactions. Since the Coulomb bound charged solitons will be freed from the impurity ions during this Mott type transition, the system enters a metallic state.

The "New Metallic Subband Model" was first proposed by Kivelson[38]. In this model, the midgap electronic bound states associated with each soliton will interact with each other and form a midgap soliton band with increasing density of solitons. At the critical concentration of dopant, the band width due to tunneling between soliton bound states becomes comparable to the disorder energy. Thus an Anderson transition from localized to delocalized state will occur and change the system into the metallic state. But to be a metallic state, this soliton band must be partially filled. In other words, there must be a finite concentration of neutral solitons in the system even in the transition range of dopant concentration. This is inconsistent with the observation of very small Curie spin susceptibility in the transition range, and the decrease in Curie susceptibility upon initial doping. Recently, based on the experiments by Chen et al.[39], Kivelson and Heeger proposed[14] a new "first-order transition to a strong-coupling polaronic metal" model. The main idea of this model can be explained by the energy band diagram in Fig.2-14. Since the creation energy of a polaron [$E_p=2^{1/2}(2/\pi)\Delta$] is bigger than a soliton [$E_s=(2/\pi)\Delta$], charge will be stored in charged soliton-antisoliton pairs during doping. This soliton lattice will form a full (for n type doping) or empty (for p-type doping) midgap band. So the energy per soliton remains unchanged during doping. For a polaron array, the upper subband in the gap is half filled. So the energy per polaron decreases as the density of polarons increases. $E_p=\surd 2(2/\pi)\Delta -(1/\pi)W_p(y)$, where $W_p(y)$ is the polaron band width. The phase transition will occur at the critical concentration that $W_p(y_c)= (E_p-E_s)=2\Delta(\surd 2-1)$. Since the upper subband of polaron is half filled, it forms a new metallic conducting subband and the system becomes a polaronic metal.

The "Commensurate-incommensurate Charge Density Wave Transition" model proposed by M.J. Rice and E.J. Mele[16] is another very interesting model. In this model, the "metallic like" state is not a real metallic state but a "gapless Peierls insulator." This gapless state was first predicted by Rice et al. [40] for the Peierls-Fröhlich conductor in which the one-dimensional system is stabilized by an incommensurate charge-density wave distortion. On account of the strong disorder in the material and the consequent short relaxation time for the charge carriers, the usual Peierls gap is replaced by a pseudo-gap so that a large density of states exists at the Fermi level. (Note the difference beween this model in which the high conductivity is due to the disorder induced density of states at Fermi level, and the model by Lee et al.[41], in which the charge current is carried by the traveling charge density wave. According to Lee, if the periodicity of the CDW is commensurate withthe lattice periodicity, the translational invariance symmetry is lost, and the CDW is pinned by the large commensurability energy. If the CDW becomes incommensurate with the lattice, the translational invariance symmetry will free the CDW for traveling and greatly increase the conductivity.) Rice and Mele applied this model to polyacetylene, and proposed that at the critical dopant concentration, the system will become a gapless Peierls insulator through the commensurate-incommurate CDW transition. Disorder and interchain coupling also play important roles in this model, narrowing the pseudo-gap, creating a finite density of states at the Fermi level, and lowering the critical concentration. An analytic formulation of this model makes several predictions: First, the density of states in the region of the Fermi energy is

$$N(E) = N_o[g + 1.5(E-E_F)^2/ \eta^2 \Delta^2 g^5] \qquad (2\text{-}64)$$

where $\eta=(h/2\pi\Delta\tau)$ is the Peierls-pair-breaking parameter, Δ is the usual incommensurate order parameter, τ is a mean electronic impurity scattering time, $g=(1-\eta^{-2})^{1/2}$ measures the reduction in the Fermi-level density of states relative to N_o, the metallic value. Second, the incommensurate distortion induces anomalous IR activity in the Raman active vibrational modes (phase phonons). These modes will be discussed later. Third, the DC conductivity is reduced from the Drude metallic value σ_o to $\delta=\sigma_o g^2$. Fourth, for $1 < \eta < 3^{1/2}$, the conductivity increases with increasing impurity scattering. The speculation is, if phonon scattering contributes to the Peierls-pair-breaking parameter as does impurity scattering, an increase in temperature, which increases phonon scattering, could lead to an increase in conductivity.

Optical Properties of Doped Polyacetylene

Infrared-active Vibrational Modes of Charged Soliton

The first specific evidence for the formation of charged solitons upon doping appears to be the infrared studies of the donor and acceptor states in lightly doped polyacetylene. In a series of experiments with various dopants, Fincher et al.[42] found that upon dilute doping two new absorption modes appeared with remarkable intensity in the IR region, at 1370 cm^{-1} and 900 cm^{-1}. The two modes are primarily polarized parallel to the chain direction, and their intensities grow in proportion to the dopant level, becoming comparable to any of the $[CH]_x$ IR absorptions at about 0.1% dopant level. Fincher et al.[42] emphasized the generality of their results; the same modes were observed for iodine, AsF_5 (p type) and for Na (n type) doping. Thus these intense absorptions are not due to specific vibrations of the dopant molecules, nor to detailed interactions between the molecules and the polymer chain. The observed generality suggests that the intense IR absorptions are intrinsic features of the charged $[CH]_x$ chain.

Motivated by these experimental results, Mele and Rice[43] developed a theory of the lattice dynamics of soliton in $[CH]_x$.

In the frequency range of the vibrational modes they found several internal modes peculiar to the soliton structure. In particular, two of these modes were found to be strongly infrared active, deriving their oscillator strength from interactions with the electrons. They showed that the dominant motions associated with the infrared-active vibrational modes of a charged soliton involve an antisymmetric contraction of the single (or double) bonds on one side of the soliton center and an expansion on the other, thus driving charge back and forth across the soliton center. Further more, they pointed out that the expected oscillator strength of the infrared-active vibrational modes of a charged soliton are large enough to be observable at very dilute doping, consistent with the experimental results, and obtained quantitative agreement with the experimental frequencies and oscillator strengths.

To describe the vibrations of the polymer, Mele and Rice[42] constructed a force-field model which consists of two principal parts. First, the "bare" nearest-neighbor bond stretching and bond-bending force constants are chosen by inspecting the characteristic vibrations of small organic complexes containing double and single C–C bonds[44]. They interpolate the dependence of the bond-stretching force constants on bond length[45] to define the force constants appropriate for the infinite polyene, and the force field thus derived is cast into the form of a Born Hamiltonian from which the bare phonons of the polyene chain are calculated. Second, they include a set of delocalized force constants derived from interactions of atomic displacements with the extended π electronic states. The importance of this electronic susceptibility for determining polyene phonon frequencies, especially those of the backbone stretching vibrations, has been discussed in the chemical literature [46-48]. Mele and Rice express this effect as a correction to the bare dynamical matrix, $\delta\ L_{\mu\nu}$, coupling displacements μ and ν with wave vector q given by:

$$L_{\mu\nu}(q) = 2 \sum_{k} \frac{\langle n,k|V_{\mu}^{*}(q)|n',k+q\rangle\ \langle n',k+q|V_{\nu}(q)|n,k\rangle}{E_{n',k+q} - E_{n,k}} \qquad (2\text{-}65)$$

where $V_{\mu}(q)$ denotes a modulation of the electronic Hamiltonian linear in the displacement μ(q) and the $|n,k\rangle$ ($|n',k\rangle$) are the filled (empty) eigenstates in the π manifold with eigenvalues $E_n(k)$ ($E_{n'}(k)$). These eigenstates are completely defined by the geometry of the chain and a constant, β, the derivative of the nearest-neighbor π-electron transfer integral with respect to bond length. (Here $\beta = \partial t/\partial u$ is the same parameter as α in reference 10 and Eq.2-2.) β is empirically adjusted to bring the screened long-wavelength C-C and C=C stretching modes in the infinite polyene into good agreement with the principal Raman peaks observed near 1080 cm^{-1} and 1474 cm^{-1} [49-51]. The calculated phonon dispersion relations below 2000 cm^{-1} are plotted in Fig.2-15[43] The results calculated from the bare-force field model are shown in Fig.2-15A. Fig.2-15B are the results calculated including coupling to π electrons (solid line) with β=8eV/Å which implies a 1.2 eV wide Peierls gap, in reasonable agreement with the 1.4 eV optical absorption threshold observed experimentally. In order to study the "kink" in an infinite chain, the matrix $\delta L_{\mu\nu}$ in coordinate space was truncated, and the open circles in Fig.2-15B were obtained by retaining terms in $\delta L_{\mu\nu}$ up to six nearest neighbors.

The coupling between the backbone modes and the π electrons will, in general, introduce into the electronic optical response functions terms in which density fluctuations in the π electron gas are coupled through the phonons, in addition to the usual interband response. This phonon induced contribution to the electronic polarizability rigorously vanishes for the neutral chain since no modulation of the nearest-neighbor one-dimensional Hamiltonian can provide a net migration of charge in the neutral chain. For the charged chain, and in particular for the charged soliton in the chain, this mechanism associates a massive oscillator strength with the ungerade internal vibrations of the defect. The calculated phonon density of states of a perfect trans-$[CH]_x$ chain projected on to the carbon displacements is shown in Fig.2-16 [43]. According to Mele and Rice, the phonons between 1000 and 1200 cm^{-1} are the skeletal modes hybridized with H bending motions; the structure between 1200 and 1400 cm^{-1} is assigned to oscillations dominated by C-C stretching character; those between 1500 and 1700 cm^{-1} are dominated by C=C stretching motions.

For a chain containing a soliton, two new considerations are raised for the local vibrational structure. Firstly, the "bare" force constants are modified as the magnitude of the bond alternation progresses smoothly through zero, changing sign at the center of the defect. Thus one anticipates vibrational modes characteristic of order 1.5 bonds localized in the defect. Secondly, in the vicinity of the kink the electronic structure is altered, and hence the electronic contribution to the dynamical matrix $\delta L_{\mu\nu}$ is locally modified. To study the roles of these two processes, a model of a charged soliton with half width $\xi=5$ CH units embedded in a 15 CH units cluster whose ends are matched to semi-infinite crystalline chains was used. The electronic corrections to the dynamical matrix were calculated to convergence within the same 15 CH units section from the eigensolutions of the infinite electronic Hamiltonian. All other screening matrix elements, i.e, those away from the kink, retained their bulk values. The vibrational structure of the central 15 CH units section of the infinite chain was evaluated numerically by applying a Green´s-function formalism to the dynamical matrix. Fig.2-17 [43] shows the local density of modes obtained from the calculation summed over carbon displacements in the section containing the charged soliton. The vertical bars labeled u_1-u_5 denote the pronounced defect-related local modes. The modes u_1 at 980 cm^{-1} and u_2 at 1360 cm^{-1} are the two most significant of these. Using the random phase approximation, the phonon coupling to density fluctuations in the π-electron gas was calculated, and the absorption coefficient associated with a concentration of 10^{19} cm^{-3} (5.4 10^{-4} per CH unit) of charged soliton defects in an unoriented film is plotted in Fig.2-18 [43]. The two modes u_1 and u_2 are remarkably infrared active. The massive oscillator strength associated with these modes may be understood as resulting from oscillations of the excess charge in the defect level in response to the lattice vibration. Upon closer inspection, it is seen that the eigenvectors u_1 and u_2 displayed in Fig.2-19 [43] describe an overall contraction on the weaker and stronger bonds, respectively, on one side of the defect and an overall expansion on the other side, thus driving charge back and forth across the defect center.

Mele and Rice claimed that these two calculated defect modes are well correlated with the dopant-induced infrared activity in $[CH]_x$ reported by Fincher et al.[42]. A strong narrow absorption at 1370 cm^{-1} and a broader, somewhat stronger absorption near 900 cm^{-1} with light doping of $[CH]_x$ with a variety of donors and acceptors were observed by Fincher et al. The integrated oscillator strengths of the observed features agree to within factors of 2-3 with those predicted by this model, normalized to an equivalent dopant level. Mele and Rice further argued that without the vibronic coupling, these effects would not be easily discernible at such low doping levels. (The 1370 cm^{-1} mode mentioned above appeared at 1390 ± 10 cm^{-1} in recent literature and is referred to as the 1400 cm^{-1} mode in this study.)

Rice and Mele[43,52] also predicted a so-called "pinning mode" which is a characteristic infrared activity associated with the oscillation of the charged soliton bound to an ionized impurity. They predicted this mode would occur at 300-500 cm^{-1}. But it never has been observed.

Horovitz has carried out similar calculations using a continuum model [53,54]. Two assumption were made in his derivation:

(a) All phonon frequencies are small compared with internal electronic transition frequencies.

(b) Lattice discreteness is neglected, i.e. $\xi \gg a$.

These two assumptions lead to the following conclusions:

(a) The IR frequencies and ratio of their intensities are independent of the charge configuration.

(b) The zero frequency translation mode acquires a finite frequency if pinning is present, from, e.g., the Coulomb interaction with the dopant ion in doped polyacetylene. The number of IR modes, including the pinning mode, equals the number of Raman modes, or the number of bare coupled phonons.

According to conclusion (a), it would be impossible to distinguish soliton and polaron excitations by the vibrational modes alone; it must be done by comparing IR intensities with interband transitions and midgap transitions or by measuring the dielectric constant. From the conclusion (b), Horovitz argued that the 900 cm^{-1} broad feature should be assigned as a pinning mode since the lowest frequency Raman mode is at 1075 cm^{-1} (or the very weak mode at 1015 cm^{-1}). No more strong infrared activity is expected at lower frequencies. The width of this absorption (about 400 cm^{-1}) at 900 cm^{-1} is attributed to a distribution of pinning parameters reflecting variations in the potential between the charged soliton and the dopant ion. This distribution is due to the variation in the distance from the pinning ion to the polymer chain. Horovitz also calculated the ratios of the oscillator strength for the two IR active features to each other and to the midgap absorption from which the effective soliton mass can be calculated.

Optical Absorptions due to Midgap Transitions

As described earlier in this chapter, the soliton energy level lies in the middle of the Peierls gap, whereas the polaron has two energy levels at $\pm\omega_0$ symmetric about the middle of Peierls gap. The optical transitions among these midgap states as well as those from the valence band to the midgap states and from midgap states to the conduction band are called midgap transitions. The theory of optical absorptions associated with the midgap transitions of soliton in the SSH model has been constructed by Horovitz[55] and Kivelson et al.[56]. Fesser et al.[25] developed a theory by using the continuum TLM model, in which the soliton and polaron excition as well as the dimerized ground state can be treated within one theoretical frame. The optical absorption coefficient $\alpha(\omega)$ was calculated in a conventional linear-response dipole approximation:

$$\alpha(\omega) = \pi\frac{\xi}{L}\frac{\Delta}{\omega} A \sum_{[1,2]} n_{1,2}|M_{1,2}|^2 \delta(\omega - \varepsilon_1 - \varepsilon_2) \qquad (2\text{-}66)$$

where the summation is over all allowed transitions from eigenstate $|1\rangle$ to eigenstate $|2\rangle$ (with energy $\varepsilon_1, \varepsilon_2$), and the matrix element $M_{1,2}$ is

$$M_{1,2} = \langle 2|\sigma_3|1\rangle$$

$$= \frac{1}{2}\int_{-L/2}^{L/2} dx[f_+^{2*}(x)\, f_-^{1}(x) + f_-^{2*}(x)\, f_+^{1}(x)] \qquad (2\text{-}67)$$

and

$$A \equiv \frac{8\pi\, e^2\, h|M_x|^2}{m^2 c\, n\, \Delta_o} \qquad (2\text{-}68)$$

where "e" and "m" are the electron charge and mass, "c" is the velocity of light, "n" is the index of refraction, and M_x is the momentum matrix element for the carbon π_z orbital[57]. The normalization to unity on a line of length L was assumed, here "L" will be taken to infinity. The factor $n_{1,2}$=0,1,2 counts the number of possible transitions allowed by occupancy of the two states. With the prefactors in Eq.2-66, the exact sum rule for optical absorption takes the form

$$\int d\omega\ \alpha(\omega) = A \tag{2-69}$$

There are three classes of transition for a soliton with one localized state in the Peierls gap and six for the polaron with two localized states. Because of the charge conjugation symmetry, the number of independent transitions reduced to two for a soliton and four for a polaron. These transitions are denoted in Fig.2-20 [25], the notation of these transitions will be refered to in this figure.

For a single soliton, the single transition (i.e., $n_{1,2}=1$) from valence band to midgap or from midgap to conduction band (see Fig.2-20b), the absorption coefficient has the form

$$\alpha_s^o(\omega) = \frac{\pi^2}{4} A \frac{\xi}{L} (\omega^2-\Delta^2)^{-1/2} \ \mathrm{sech}^2[\frac{\pi}{2\Delta} (\omega^2-\Delta^2)^{1/2}] \tag{2-70}$$

so that

$$\int_\Delta^\infty \alpha_k^o(\omega)\ d\omega = 1.41 \frac{\xi}{L} A \tag{2-71}$$

Due to the matrix element symmetry, the total absorption from transitions between extended and localized states is twice that in Eq.2-70 and Eq.2-71, independent of the midgap occupation. The interband absorption coefficient in the presence of a soliton cannot be given analytically. As pointed out by Kivelson[56], although the soliton is a local excitation, it results in a global change in the dimerization of the system. This alters the phase relations in the valence and conduction bands, causing diagonal transitions (k=0) to be explicitly forbidden. But for high frequency ($\omega>2.5\Delta$), weight is removed uniformly in ω with respect to the pure dimerized (D) case. Thus one has

$$\alpha_S^{IB} \simeq \alpha_D(\omega)\ (1-2\ \xi/L) \qquad (2\text{-}72)$$

where $\alpha_D(\omega)$ is the interband absorption for the pure dimerized case given by

$$\alpha_D(\omega) = A(2\Delta/\omega)^2\ (\omega^2 - 4\Delta^2)^{-1/2} \qquad (2\text{-}73)$$

Using the polaron solutions for Eq.2-27 in Eq.2-66, Fesser et al.[25] calculated all of the four transitions for the single polaron: α_p^1 is due to the transition between the lower and upper localized polaron states; α_p^2 is due to the transition from the valence band to the lower polaron level or from the upper polaron level to the conduction band; α_p^3 is due to the transition from the valence band to the upper polaron level or from lower polaron level to the conduction band; α_p^{IB} is due to the interband transition. The relative intensities of the three midgap transitions are shown in Fig.2-21 [25] as a function of the polaron energy level ω_o. The optical-absorption spectrum (in arbitrary units) below the Peierls gap $\omega=2\Delta$ with a Gaussian broadening of $\sigma=0.14$ calculated for single soliton, single electron polaron with $\omega_p=2^{-1/2}\Delta$ and single bipolaron with $\omega_{bp}=0.65\Delta$ are shown in Fig.2-22, Fig.2-23 and Fig.2-24 [25].

So far, most of the important theories of polyacetylene have been introduced in this chapter. In this dissertation, we will focus on three important problems: first, we try to discriminate between the hopping model and the diffussive charged soliton model for lightly and intermediately doped trans-$[CH]_x$; second, we attempt to answer the question of whether heavily doped polyacetylene is a metallic state or not; and third, we examine the three models for the insulator-conductor transition by optical and conductivity measurements.

Table 2-1

Conjugational Defects as Quasi-particles in Polyacetylene

Defect	Charge	Spin	ω_o	$k_o v_F$	ξ	E
Soliton	+e	0	0	Δ_o	v_F/Δ_o	$2\Delta_o/\pi$
	0	1/2				
	−e	0				
Polaron	e	1/2	$2^{-1/2}\Delta_o$	$2^{-1/2}\Delta_o$	$2^{1/2}v_F/\Delta_o$	$2\times2^{1/2}\Delta_o/\pi$
	−e	1/2				
Bipolaron	+2e	0	$0 < \omega < 2^{-1/2}\Delta_o$			
	−2e	0				

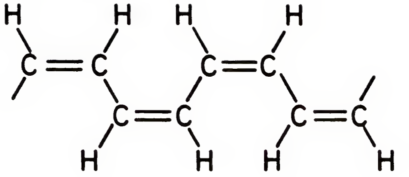

CIS

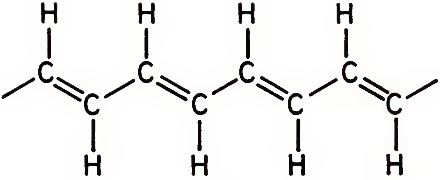

TRANS

Figure 2-1
Polymer Chain Structure of Cis- and trans-$[CH]_x$.

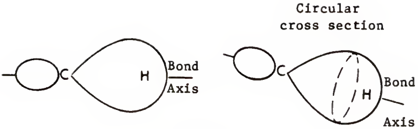

σ bond

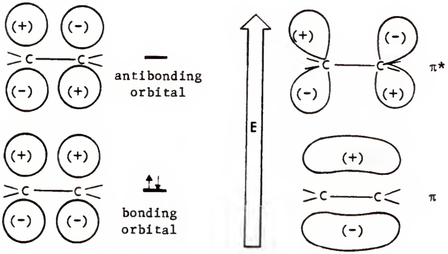

The interaction of P orbitals to form the bonding and antibonding molecular orbitals of a π bond.

Figure 2-2
σ bond and π bond.

From reference 18 page 210

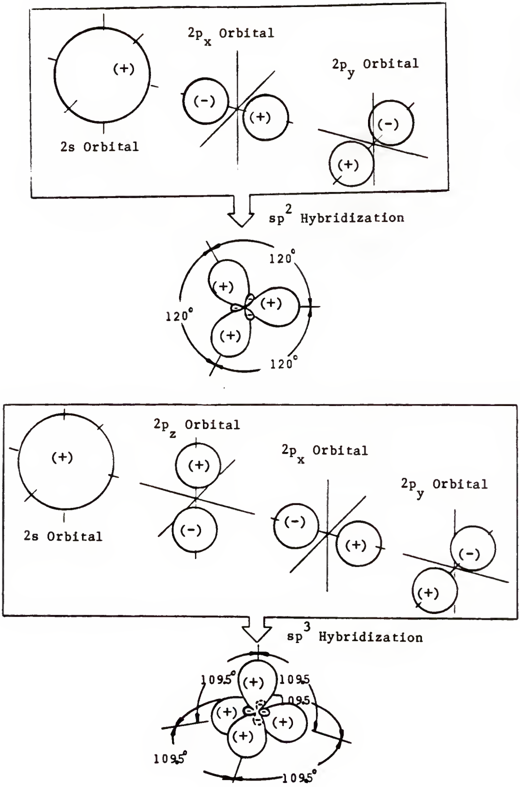

Figure 2-3

sp^2 and sp^3 hybridization.

From reference 18 page 33

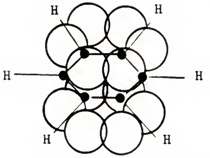

Overlapping P orbitals in benzene.

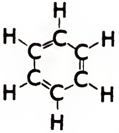

The Kekule formula for benzene

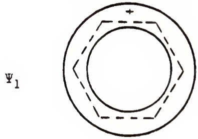

Shapes of the π molecular orbitals of benzene as viewed from above.

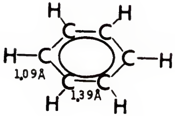

Bond lengths in benzene.

Figure 2-4
Extended π bond in benzene.

From reference 18 page 442

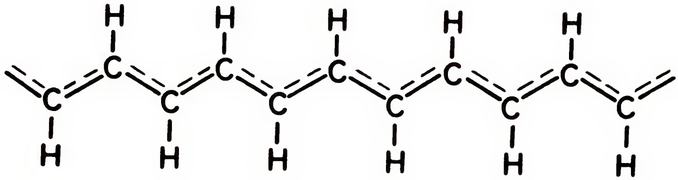

Figure 2-5
Trans-$[CH]_x$ with uniform bond length.

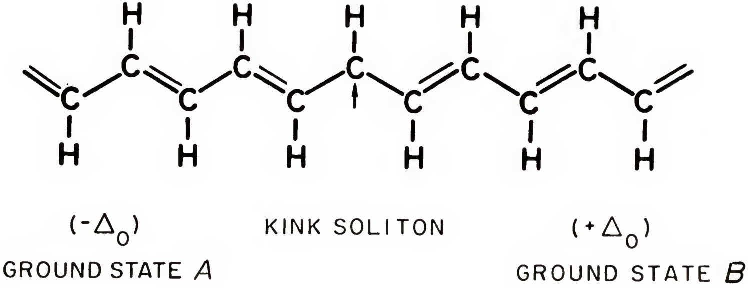

Figure 2-6
Two degenerate ground state and topological soliton in trans-$[CH]_x$.

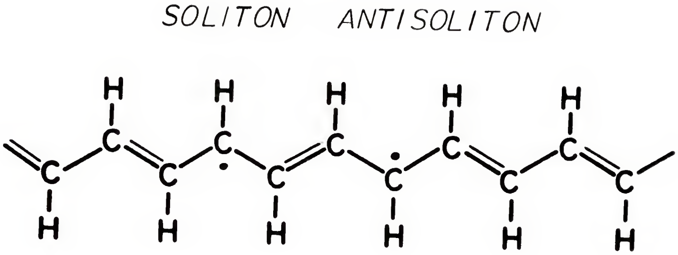

Figure 2-7
Soliton and antisoliton in trans-$[CH]_x$.

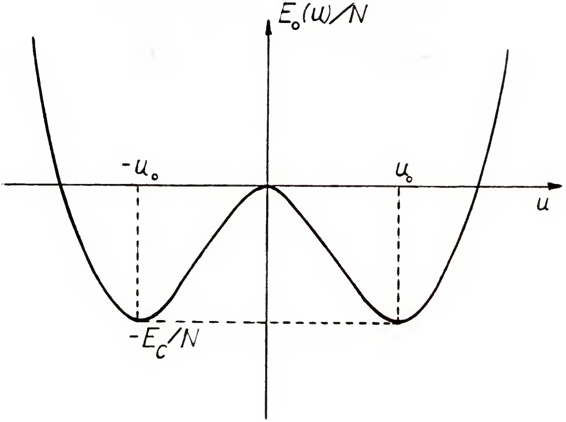

Figure 2-8
Born-Oppenheimer energy per CH group as a function of the staggered dimerization coordinate u.

From reference 10

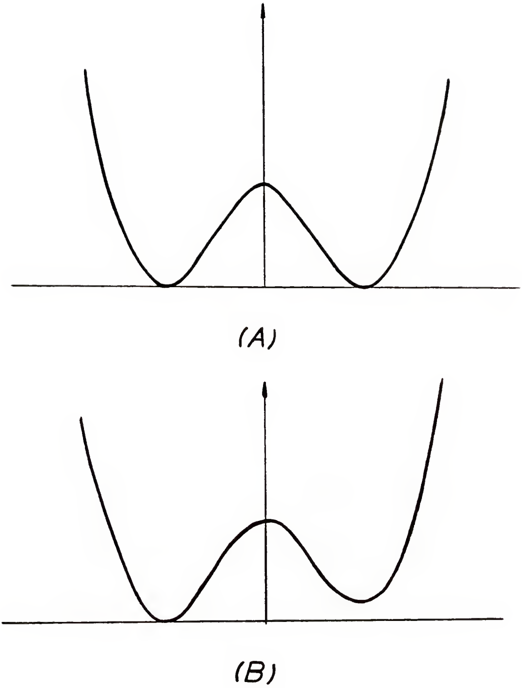

Figure 2-9

Potential in a ϕ^4 like nonlinear equation
(A) Degenerate (B) Symmetry broken

From reference 21

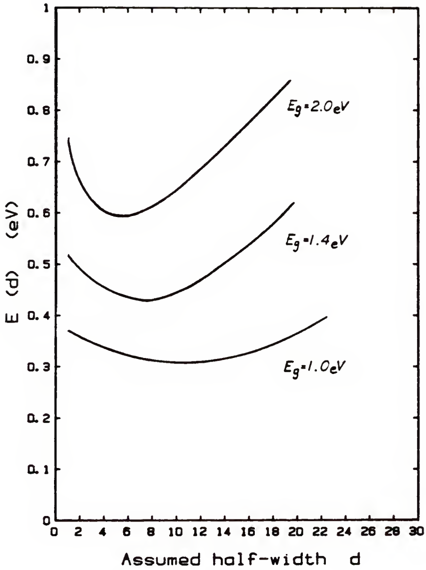

Figure 2-10
Soliton energy E(d) as a function of an assumed half-width d for several values of the energy gap E_g.

From reference 10

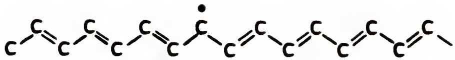

neutral soliton

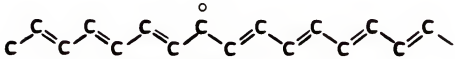

positively charged soliton

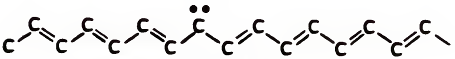

negatively charged soliton

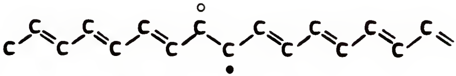

positively charged polaron

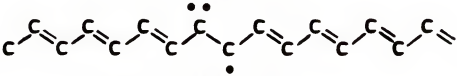

negatively charged polaron

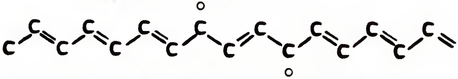

positively charged Bi-soliton (Bi-polaron)

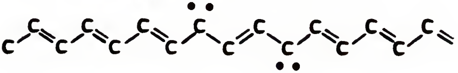

negatively charged Bi-soliton (Bi-polaron)

Figure 2-11
Topological feature of conjugational defects in $[CH]_x$.

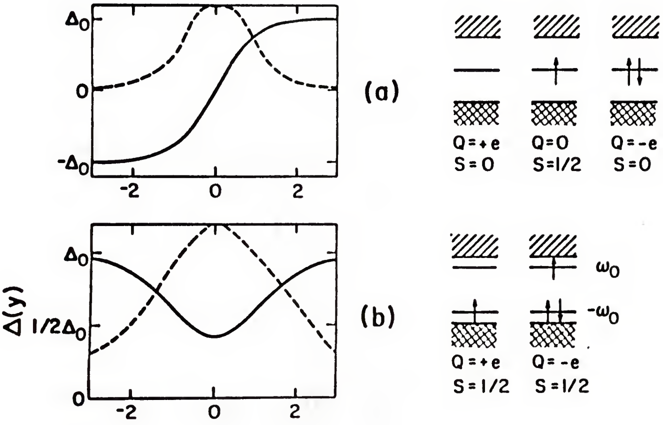

Figure 2-12
Order parameter (Solid line) and wavefunction (dashed line) and electronic spectrum of (a) soliton (b) polaron

From reference 25

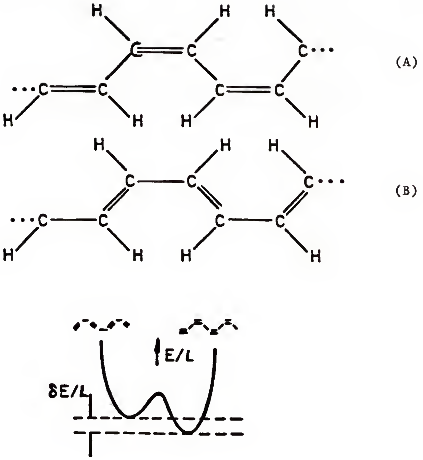

Figure 2-13
Schematic of cis-polyacetylene lattice and potential energy
(A) trans-cisoid (B) cis-transoid

From reference 25

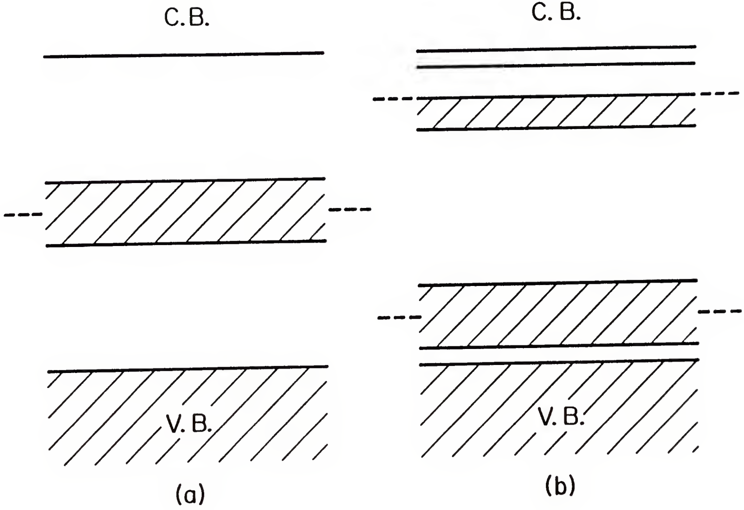

Figure 2-14
(a) Band diagram for a soliton lattice; the midgap band is full(n-type doping)
(b) Band diagram for a polaron lattice; the upper palaron band is half-full (n-type doping)

From reference 14

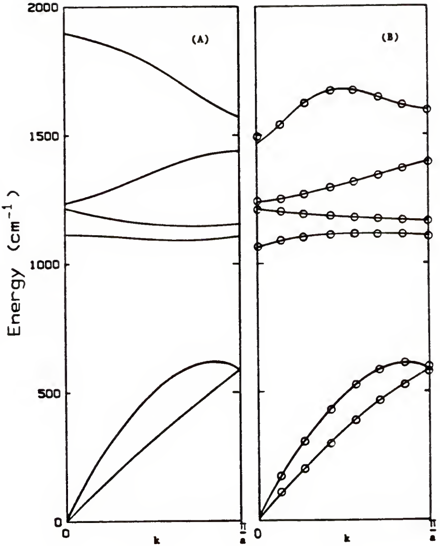

Figure 2-15
In-plane vibrations below 2000 cm^{-1} in trans-$[CH]_x$.

(A) Calculated from the bare-force-field-model.
(B) Phonons calculated including coupling to π electrons (solid curve); phonons obtained by truncating the delocalized force field after sixth nearest neighbors (open circles).

From reference 43

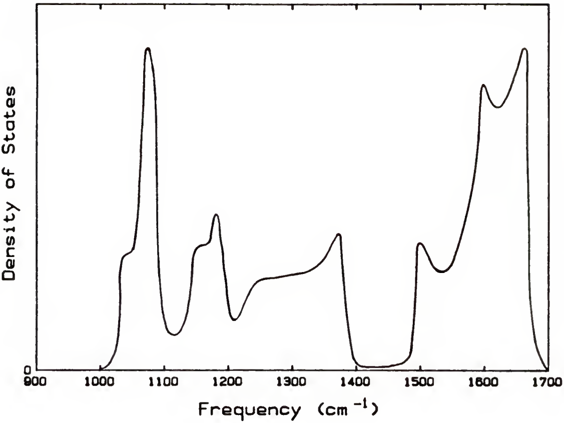

Figure 2-16
Projected phonon density of states
for carbon motions in trans-$[CH]_x$.

From reference 43

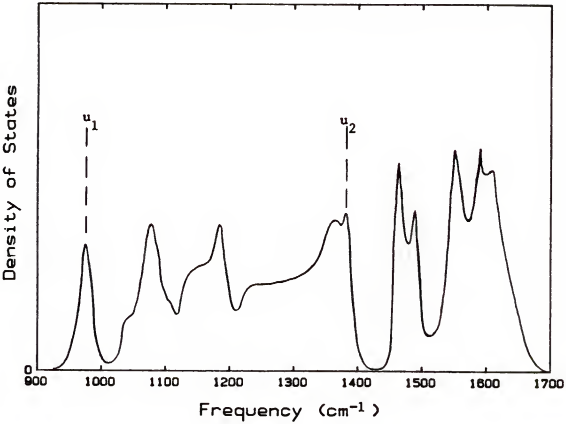

Figure 2-17
Projected phonon density of states averaged
over 15-atom section containing a soliton

From reference 43

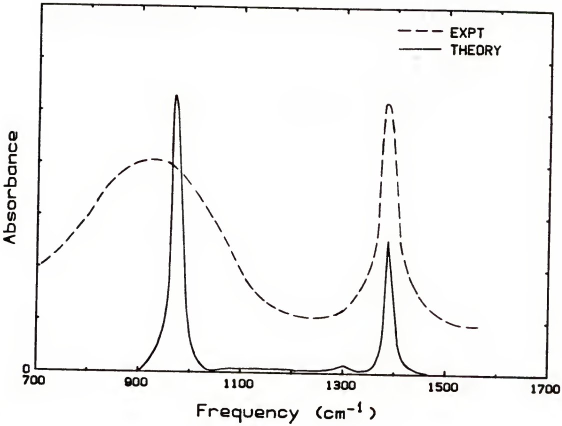

Figure 2-18
Absorption coefficient calculated for 10^{19} cm^{-3} of soliton defects.

From reference 43

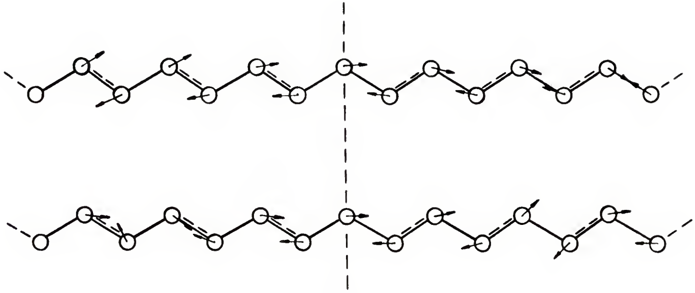

Figure 2-19
Normal modes for the u_1 and u_2 vibrations.

The vertical dashed line marks the center of the soliton with the even bonds as counted from the center becoming increasingly strong

From reference 43

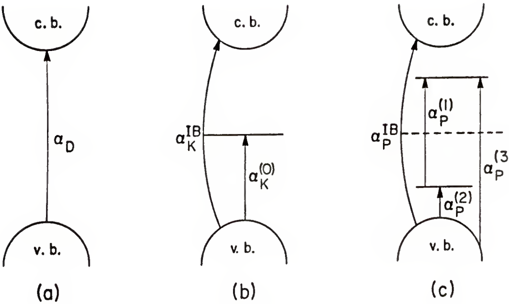

Figure 2-20
Nomenclature for all possible different transitions:
(a) dimerized chains (b) single soliton (c) single polaron

From reference 25

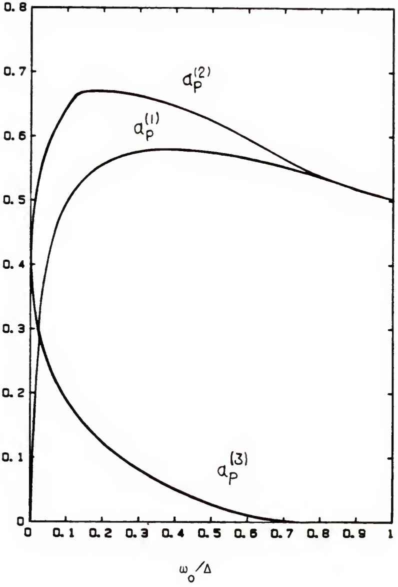

Figure 2-21
Integrated weights of single transitions involving localized levels as a function of ω_o

From reference 25

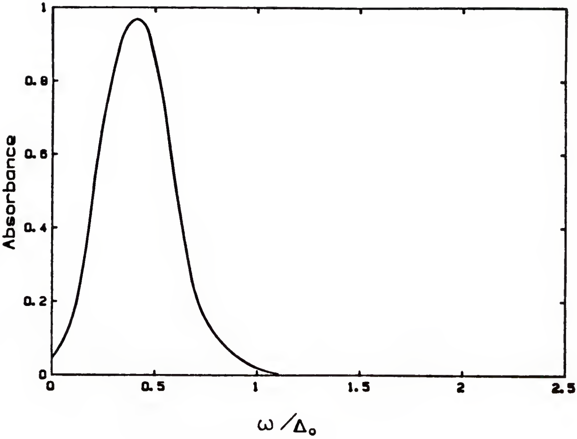

Figure 2-22
Optical absorption spectrum (arbitrary units) below the gap $\omega=2\Delta_o$ with a Gaussian broadening of $\sigma=0.14\Delta_o$ for a single soliton

From reference 25

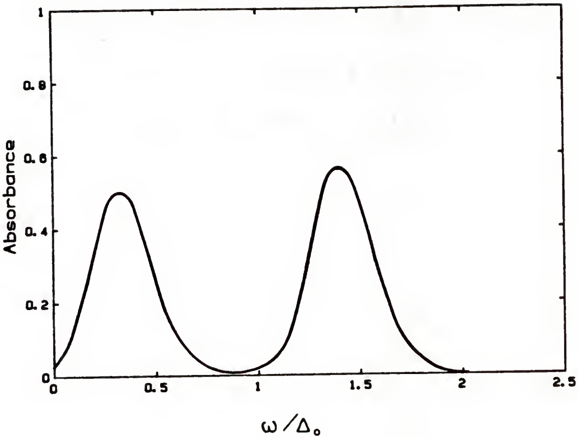

Figure 2-23
Optical absorption spectrum (arbitrary units) below the gap $\omega=2\Delta_0$ with a Gaussian broadening of $\sigma=0.14\Delta_0$ for a single electron polaron with $\omega=\Delta_0/\sqrt{2}$ (for trans-$[CH]_x$).

From reference 25

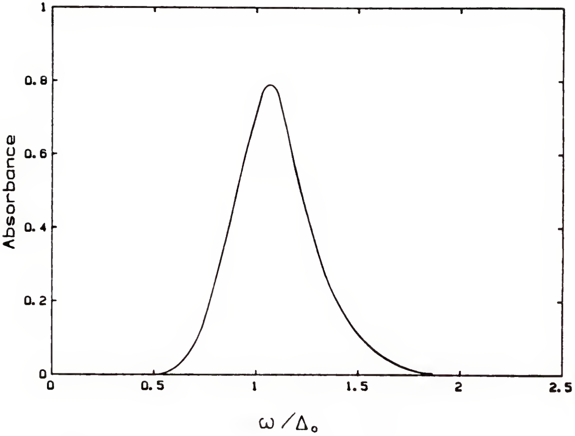

Figure 2-24
Optical absorption spectrum (arbitrary units) below the gap $\omega=2\Delta_o$ with a Gaussian broadening of $\sigma=0.14\Delta_o$ for a single bipolaron with $\omega_o=0.65\Delta_o$.

From reference 25

CHAPTER III
OPTICAL TECHNIQUES

The Monochromator

Reflection and transmission measurement were made in the 700–25000 cm^{-1} frequency range using a spectrometer built around a Perkin-Elmer model 16 U grating monochromator. It will be referred to as the PE spectrometer throughout this dissertation. A diagram of the spectrometer is shown in Fig.3-1. A globar light is the source used in the 700 to 4400 cm^{-1} frequency range; a quartz tungsten bulb is the source from 4400 to 27000 cm^{-1}; and a deuterium arc lamp can be used to cover the range from 26000 to 45000 cm^{-1}. The proper source can be selected from outside the vacuum tank by turning M2. Low-pass and band-pass filters are used to eliminate undesired orders of diffraction. A grating and two small openings called slits are used in this monochromator. Details about the grating monochromator will be disscussed later.

A large spherical mirror images the exit slit of the monochromator onto either a reference mirror or a sample (for reflection measurements). A second spherical mirror, matching the first, images the reflected light at the far focus of an ellipsoidal mirror which in turn focuses the light onto the detector. For transmission measurements the sample is placed at the focus position of the second spherical mirror. The detector for the 700 to 4000 cm^{-1} frequency range is a thermocouple with a KBr window while an ambient temperature PbS photoconductor can be used from 4000 to 20000 cm^{-1}, and a photomultiplier can be used for the range of 20000 to 47000 cm^{-1}. The vacuum tank must be vented for changing detectors. Since polyacetylene is degraded by oxygen, the thermocouple was used to cover the entire frequency range from 700 to 25000 cm^{-1} in this work in order to reduce the probability of exposing the sample to oxygen.

Polarizers can be placed after the exit slit and before the focus of the second spherical mirror if polarized reflectance or transmission measurements are required. Wire grid polarizers on calcium floride or KRS5 are used in the mid infrared, dichroic polarizers are used in the near infrared, and plastic polarizers are used in the visible region. Each polarizer can be placed in or out of the beam path and can be positioned at the appropriate angle by using remote controls passing through the vacuum tank wall. The orientation of the polarization can be read by a digital display.

The light signal is chopped to give it an AC component which can then be amplified by an Ithaco model 393 lock-in amplifier. The output signal from the lock-in is fed into an integrating digital voltmeter (DVM) with a digital interface. The data is sent through this interface over the guard crossing to the digital controller and then processed as required for transmission. The data is transmitted through the IEEE-488 Bus and a general purpuse interface box(GPIB) from the DVM to a PDP 11-23 computer and recorded on an 8" floppy disk.

The function of the grating monochromator is described by the grating equation which can be derived from the ray diagram in Fig.3-2 [58]:

$$m\lambda = d(\sin i + \sin \delta) \tag{3-1}$$

where "m" is the order of diffraction, "d" is the grating constant (cm/line), "i" is the angle of the incident light and "δ" is the angle of the diffracted light. The angle "i" and "δ" are both measured with respect to the normal vector to the plane of the grating. Eq.3-1 can be rearanged into

$$m\lambda = 2d \sin\frac{i+\delta}{2}\cos\frac{i-\delta}{2} \tag{3-2}$$

$$m\lambda = 2d \cos(\varepsilon) \sin(\varepsilon) \tag{3-3}$$

$$m \operatorname{cosec}(\theta) = 2d \cos(\varepsilon)\ \omega \tag{3-4}$$

where $2\sigma=i-\delta$ is the angle between incident and diffracted beam determined by the geometry of the optical path (see Fig.3-2). $\theta=0.5(i+\delta)$ is the rotating angle of the grating with respect to zero-order position, and $\omega=1/\lambda$ is the wave number. When θ is small, Eq.3-4 can be approximated as

$$m \operatorname{cosec}(\theta) \approx 2d\omega \qquad (3\text{-}5)$$

The rotating angle of grating scans from 60 degrees to about 15 degrees, corresponding to so-called "drum number" from 0 to 24. The gratings were calibrated by passing the light from a HeNe laser (ω =15803cm^{-1}) through the monochromator and observing the different orders of diffraction. The data were fit with a third degree polynomial. Table 3-1 lists the equation and parameters which were used to calculate the wave numbers from the drum numbers on the grating monochromator.

The grating is driven by a computer controlled stepping motor. By setting the impulses per second (IPS) to 80, and using a 1:4 gear reduction (numbered 8 on the panel), 10 points of data will be taken for every one drum revolution (one drum number increment). According to table 3-1, this corresponds to ω_{sp}=5.4cm^{-1} for the 101 grating and ω_{sp}=78.9cm^{-1} for 1440 grating. This spacing is good enough for work on most solid state material. Finer spacing can be achieved by reducing the IPS. However, the limitation on resolution depends on the width of the slits. The frequency bandwidth is

$$\Delta\omega = \frac{\omega\ s\ \mathrm{ctn}(\theta)}{2F} + \frac{\omega\ d\ h(\alpha)}{W\ m} \qquad (3\text{-}6)$$

where "s" is the slit width, "F" is the focal length of the collimator mirror (26.7 cm), "θ" is the angle of grating, "W" is the width of the collimated beam (3.4 cm), "m" is the order of diffraction, $h(\alpha)$ is an error function for the slit and α=S W ω/F. The first term in Eq.3-6 is due to the physical slit. It can be derived from Eq.3-3 for m=1 as follows:

$$\lambda = 2d\ \cos(\varepsilon)\ \sin(\theta) \qquad (3\text{-}7)$$

$$\Delta\lambda = 2d\ \cos(\varepsilon)\ \cos\ (\theta\ )\Delta\theta \qquad (3\text{-}8)$$

$$\Delta\omega = \Delta(1/\lambda) = \lambda^{-2}\Delta\lambda \qquad (3\text{-}9)$$

$$\Delta\omega = 2\omega\ \mathrm{ctn}(\theta)\Delta\theta \qquad (3\text{-}10)$$

But

$$\Delta\theta = S/F \qquad (3\text{-}11)$$

so

$$\Delta\omega = \frac{\omega\ s\ \mathrm{ctn}(\theta)}{2F} \qquad (3\text{-}12)$$

The second term in Eq.3-6 is due to the ultimate resolving power of the grating. Theoretically, this resolving power is equal to the number of wave lengths per path difference, taken between the rays that are diffracted from the opposite extreme ends of the grating (W) into the direction θ. This theoretical value is not reached because of the diffraction limit of the optical system of the monochromator, its aberration and energy limitation. The maxmum opening of the slit is 0.2 cm, so with $s=0.2$ and $F=26.7$ cm, Eq.3-12 gives $\Delta\omega/\omega=0.2\%$ for $\theta=60^{\circ}$ (drum number 0), and $\Delta\omega/\omega=1.4\%$ for $\theta=15^{\circ}$ (drum number 24). More detailed information about the grating monochromator can be found in reference 59. The operating parameters of the PE spectrometer are listed in table 3-2.

In order to measure the reflectance of a large number of polyacetylene film samples precisely and efficiently, a specially designed sample holder was used as shown is Fig.3-3. The sample rotator is mounted on a X-Y-Z slide station. By turning the rotator by a steel wire cable which passed through the wall of the vacuum tank, the reference mirror and three samples can be put into the beam one by one. A spring-loaded pin will hold the possition of each sample precisely. The fine adjustment can be made by moving the rotator along the three independent directions of the slide station.

A clear plastic lid with two rubber gloves is used as one of the three lids on the vacuum tank, so the whole tank becomes a glove box with the spectrometer in it. In order to minimize the possibility of oxidation of polyacetylene the tank is evacuated after putting the tools, sample holders and sample glass tubing in it. When the vacuum reaches 300 m torr, the tank is vented and then purged by nitrogen gas. Breaking the sample glass tubing, mounting or dismounting samples, and adjusting the optical system can all be done through the gloves while the sample is being protected by the nitrogen gas. As shown in Fig.3-4, the aluminum cap rests at the countersink of an aluminum flange at the bottom of the glove chamber when the tank is under vacuum. A rubber sheet covers the gap between the cap and the flange to prevent damage to the gloves by the pressure difference between the vacuum and atmosphere. This cap can be removed through the slot and set in the tank in order to use the gloves when purging nitrogen gas. The cap must be put back before evacuating the tank.

The Interferometer

Reflection in the 50-700 cm^{-1} frequency range was measured by a Michelson interferometer. The basic principle of Michelson interferometry can be briefly described as follows. A beam from a wide band source is divided into two arms by a beamsplitter with one part reflecting from a fixed mirror and the other reflecting from a movable mirror. Before reaching the detector, the two beams recombine with a phase different $\phi=kx$. Here $k=2\pi/\lambda$ and x is the path difference between the arms. For each monochromatic component of the wideband source, the electric field amplitude of the recombined beam is

$$E_R(z_1 z_2,k) = rtE_o(k)[e^{-i(\omega t-kz_1)} + e^{-i(\omega t-kz_2)}] \qquad (3\text{-}13)$$

where "r" is the reflection coefficient, "t" is the transmission coefficint of the beamsplitter, and z_1 and z_2 are the distances traveled by the two beams. The intensity of the beam is

$$I(z_1,z_2,k) = E_R(z_1,z_2,k)\ E_R^*\ (z_1,z_2,k)$$

$$= 2E_o^2\ (k)|rt|^2\ [1+\cos(z_1-z_2)k] \qquad (3\text{-}14)$$

so the total intensity at path difference $x=z_1-z_2$ is

$$I(x) = 2|rt|^2[\int_o^\infty E_o^2(k)dk + \int_o^\infty E_o^2(k)\cos(kx)dk] \tag{3-15}$$

For x approaching infinity, cos(kx) will oscillate rapidly, so the second term will vanish. We have

$$I(\infty) = 2|rt|^2\int_o^\infty E_o^2(k)dk = \frac{1}{2}I(0) \tag{3-16}$$

The interferogram is the difference between I(x) and I(∞),

$$I(x) - I(\infty) = 2|rt|^2 \int_o^\infty E_o^2(k)\cos(kx)dk \tag{3-17}$$

The spectrum is the cosine Fourier transform of the interferogram

$$S(k) = E_o^2(K) = C\int_o^\infty [I(x) - I(\infty)]\cos(kx)dk \tag{3-18}$$

where C is a constant. Providing

$$S^*(k) = S(-k) \tag{3-19}$$

Eq.3-18 can be written as

$$S(k) = C \int_{-\infty}^{\infty} [I(k) - I(\infty)]\, e^{ikx}\, dk \qquad (3\text{-}20)$$

so by using a Fast Fourier Transform (FFT) program, we obtain the spectrum.

But it is impossible to measure the interferogram continuously over infinite path difference; in practice, it is measured at an evenly spaced finite number of points. The finite length causes side lobes near sharp spectral structures which can be eliminated by the technique of apodization[60] at a cost of degraded resolution. The path difference sampling interval must be small enough to prevent aliasing, in which the high frequencies appear to be lower frequencies. The interval "Δx" must satisfy $\Delta x < (2\omega_{max})^{-1}$, where ω_{max} is the maximum wave number used in the spectrum. Also, cutoff filters are used to remove the higher frequency components. The resolution in the spectrum, $\Delta\omega$, is determined by

$$\Delta\omega = C/L \qquad (3\text{-}21)$$

where "L" is the maximum path difference, "C" varies from 0.5 to 1 depending on apodization procedure and the different definition of $\Delta\omega$.

A diagram of the Michelson interferometer is shown in Fig.3-5. The light source is a mercury arc lamp. The beam is chopped in order to use a phase sensitive amplifer. Stretched mylar beamsplitters of thickness 0.1 mil and 0.5 mil are used to cover 30 to 700 cm^{-1}. The movable mirror is driven by a computer controlled stepping motor in multiples of 0.3164 microns increment.

A doped germanium bolometer cooled by liquid helium is used as a detector. By pumping the helium bath in the detector can, 1.2 K can be reached, resulting in a very good signal to noise ratio. A set of filters, located near the detector, is used to eliminate undesired high frquencies. Fig.3-6 shows a diagram of the cryostat. The signal from the detector is amplified and recorded on computer diskettes in the same manner as described in the monochromator section.

Table 3-1

Drum to Wave Number Parameters

$$\text{Wave number}(\mathrm{cm}^{-1}) = A + B*DRUM + C*DRUM^2 + D*DRUM^3$$

Grating (lines/mm)	A	B	C	D
30	170.351	16.017	-0.0107	-0.000245
40	231.345	21.533	0.0272	-0.00068
101	584.203	54.418	0.0508	-0.00124
240*	1387.533	130.572	0.0776	-0.00159
640#	3696.487	347.897	0.0	0.0
1440#	8280.0	789.4	0.0	0.0
2880	16560.0	1578.8	0.0	0.0

*Data fit with first degree polynomial.

#Data from Perkin-Elmer.

Table 3-2

Monochromator parameters.

Wavenumbers	Drum	Grating	Slit Width	Filters		Polarizers	Detector
(cm^{-1})	Numbers	(lines/mm)	(microns)	L	H	A B	& Source
510- 710	13-22	40	1750	2	0	Grid/Blank	Thrm/Glo
690- 1020	2- 8	101	1750	3	0	Grid/Blank	Thrm/Glo
910- 1570	7-18	101	1500	4	0	Grid/Grid	Thrm/Glo
1520- 1900	17-24	101	1500	5	0	Grid/Grid	Thrm/Glo
1780- 2570	3- 9	240	1750	5	0	Grid/Grid	Thrm/Glo
2430- 4410	8-23	240	1250	6	0	Grid/Grid	Thrm/Glo
4400- 5780	2- 6	640	50	7	0	IR/Grid	PbS/W
5780- 8570	6-14	640	20	7	0	IR/IR	PbS/W
8280-13000	0- 6	1440	50	0	1	IR/IR	PbS/W
12200-15400	5- 9	1440	100	0	2	Vis/Vis	PbS/W
14600-20700	8-16	1440	15	0	3	Vis/Vis	Photo/W
19300-25000	14-21	1440	20	0	4	Vis/Vis	Photo/W
24000-27000	20-24	1440	100	0	6	Vis/Vis	Photo/W
26000-32000	6-10	2880	450	0	5	Vis/Vis	Photo/D2
31000-38600	9-14	2880	450	0	6	Vis/Vis	Photo/D2
35000-47000	13-19	2880	850	0	7	vis/Vis	Photo/D2

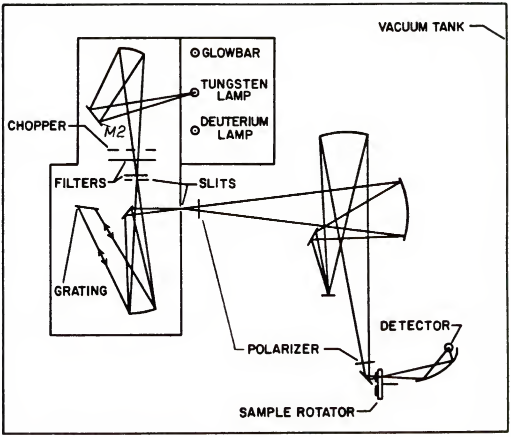

Figure 3-1
Schematic diagram of grating monochromator spetrometer.

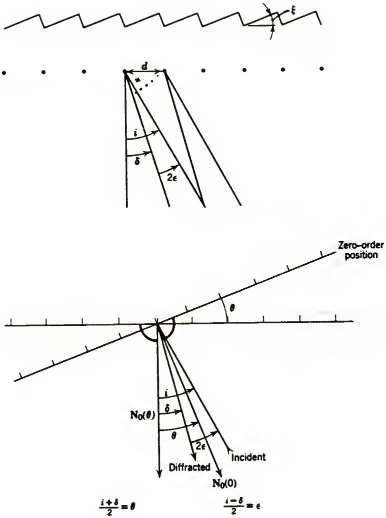

Figure 3-2
Ray diagram of grating.

From reference 58

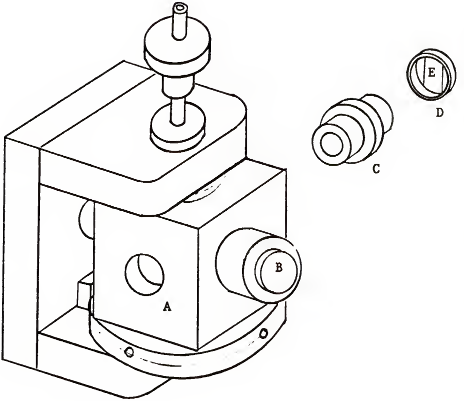

A Rotator
B Reference mirror
C Sample holder
D Sample holder ring
E Sample

Figure 3-3
Sample rotator for reflectance measurement.

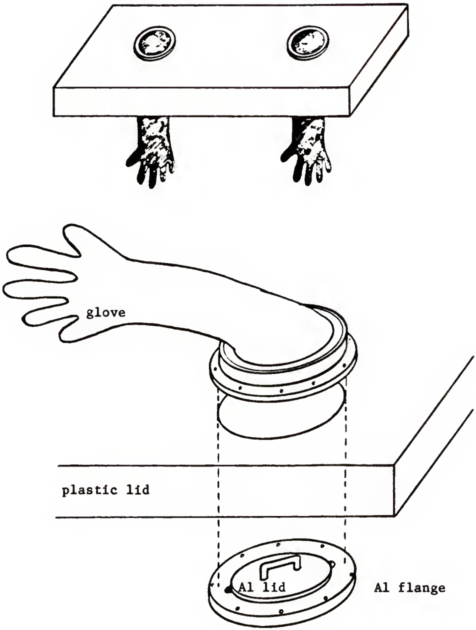

Figure 3-4
Rubber gloves attached to plastic lid.

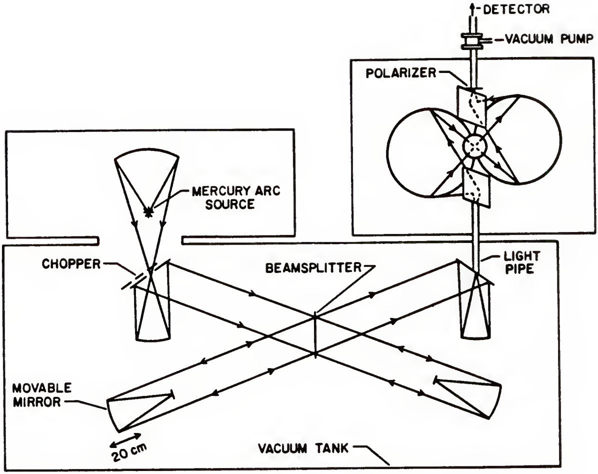

Figure 3-5
Schematic diagram of Michelson interferometer.

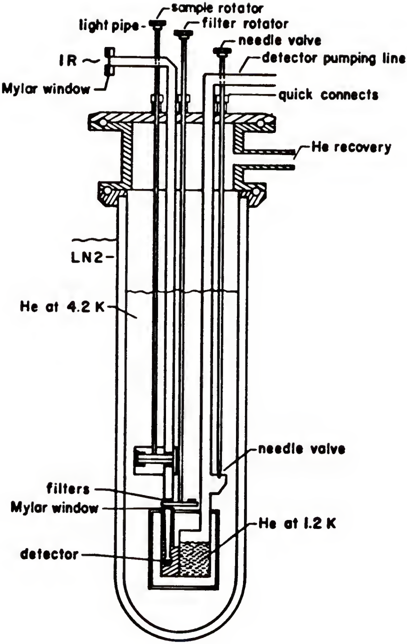

Figure 3-6
Schematic diagram of He cryostat for bolometer detector.

CHAPTER IV
DATA AND RESULTS

Segmented Polyacetylene-$[CHD_y(I_3)_z]_x$

To find whether the dominating effect for conductivity is one-dimensional diffusion of charged solitons or three-dimensional hopping, the charge transport and optical properties of segmented polyacetylene were studied. Segmented polyacetylene is made by introducing sp^3 hybridized defects on the polymer chains in a controlled manner, so that polyacetylene chains with average conjugation length of order 1000-10000 C-H units can be chopped into shorter segments. Various average conjugation lengths can be obtained by controlling the concentration of sp^3 defects.

Sample Preparation

The segmented samples were prepared by a research group at the University of Pennsylvania. Sample preparation according to reference 61 was done in the following way. The $[CH]_x$ samples were prepared as the cis-isomer by the Shirakawa method [5], and then isomerized to trans-$[CH]_x$ by heating in a purified argon atmosphere for 90 minutes at 140°C. The samples are free standing films with 100 microns average thickness and have the form of a matted network of fibrils of 200Å average diameter. The method of introducing sp^3 defects is a variation of the technique used by Pron [62], Soga et al.[63], and Furukawa et al.[64]. The apparatus used is shown in Fig.4-1. The film was first n-doped by sodium using a sodium naphthalide solution. After doping, the film was washed by repeated internal distillation of tetrahydrofuran (THF), and dried by a cryopumping technique. Then the sodium doped sample was compensated by deuterated alcohol (either CH_3CH_2OD or CH_3OD) through vapor phase reaction. Following compensation, the film was washed by alcohol. The chemical reactions involved are

$$[CH]_x + xyNa^+(NaPhth)^- \rightarrow [Na_y^+ (CH)^{-y}]_x + xy(NaPhth) \qquad (4\text{-}1)$$

$$[Na_y^+ (CH)^{-y}]_x + xyROD \rightarrow [CHDy]_x + xyRONa \qquad (4\text{-}2)$$

This two-step method of introducing sp^3 defects on polyacetylene chains is sketched in Fig.4-2.

Soga [63] has shown that the uptake of protons (or deuterons) is equal to the amount of sodium in the $[Na_y^+(CH)^{-y}]_x$ films. Thus, a very accurate measurement of y may be made by titration of the alcohol solution resulting from Eq.4-2. All values of y given in this dissertation were determined by titration of this solution with 0.01 molar HCl, using a phenolphthalein indicator. Assuming a homogeneous distribution of sp^3 conjugated defects, the average conjuagtion length can be simply expressed as L=1/y (in C-H unit). After drying, the light golden color films were sealed in evacuated glass tubes and shiped to Xerox Webster Research Center where the iodine doping and conductivity measurements were carried out by me.

The apparatus used for lightly iodine doping is shown in Fig.4-3. After exposing the polyacetylene to the I_2 vapor for a short time (2-3 seconds), the vessel was pumped out for 48 hours and the conductivity was monitored to assure that equilbrium had been reached. The dopant concentration was determined by weight uptake. Most of the sample handling, such as doping, weighing, and mounting on the conductivity apparatus were performed in an argon atmosphere glove box.

Frequency and Temperature Dependent Conductivity.

The sample chamber shown in Fig.4-4 was used. To protect the sample from oxidation, the sample chamber was sealed and the pressure of argon gas inside of the chamber was kept above one atomosphere. A thermocouple was attached on the copper plate where the sample was mounted to monitor its temperature. In order to reduce contact resistance, gold electrodes were evaporated onto the samples. The sandwich cell configeration (Fig.4-5a) was used for undoped $[CHD_y]_x$. Two parallel stripe type electrodes (Fig.4-5b) were used to measure the conductivity along the length of doped $[CHD_y(I_3)_z]_x$ samples. The frequency dependent conductivity was obtained at each fixed temperature using a General Radio Capacitance-Conductance Bridge. The DC. Conductivity was obtained using a Keithley high impedance electrometer. The temperature was varied by controlling the liquid nitrogen flow (cooling) or the power to the heater in an oven containing the sample chamber (heating).

The experimental results for $\sigma(f,T)$ of $[CHD_y(I_3)_z]_x$ are plotted in Fig.4-6 and Fig.4-7 for y=0.02 samples, Fig.4-8 and Fig.4-9 for y=0.17 samples. In order to compare these properties of short chain polyacetylene to ordinary $[CH]_x$, the results of Epstein et al.[65] for $\sigma(f,T)$ of trans-$[CH]_x$ and ammonia compensated $[CH]_x$ are plotted in Fig.4-10 and Fig.4-11 respectively, and the $\sigma(f,T)$ of amorphous silicon [66] is plotted in Fig.4-12. It is no surprise that the frequency and temperature dependence of the conductivity for both undoped and doped y=0.02 samples is similar to trans-$[CH]_x$. There is a strongly temperature-dependent DC conductivity; the frequency dependence becomes significant only at very low temperature. This behavior indicates that a low concentration of sp^3 defects (y=0.02) does not qualitatively change the charge transport mechanism. However, the room temperature DC conductivity is reduced by a factor of 10^{-4} from the ordinary trans-$[CH]_x$.

The result for undoped y=0.17 sample is completely different from the y=0.02 and conventional trans-$[CH]_x$ samples. The temperature dependence of the DC conductivity is weaker; it increases by a factor of 1000 as temperature increases from 170K to 347K (compared to a factor of 10^5 for the undoped y=0.02 sample). Furthermore, the frequence dependence of conductivity is very strong even at temperatures as high as 300 K. This behavior resembles cis-$[CH]_x$ as well as ammonia compensated trans-$[CH]_x$. It is very interesting that after very light doping (z=0.00051), the y=0.17 sample recovered all features of conventional trans-$[CH]_x$, but the room temperature DC conductivity is only 1/10 of that for y=0.02 sample with the same dopant concentration (which in turn is smaller than ordinary trans-$[CH]_x$).

Kivelson and Epstein [33] have developed a method to distinguish two types of hopping in charge conduction: isoenergetic hopping, where the distribution of site energies is narrow on the scale of k_BT; and variable-range hopping, in which the distribution is much broader than k_BT. The results can be summerized as follows. For isoenergetic hopping,

$$\frac{\sigma(\infty)}{(0)} = \frac{9D}{32\pi A}\left(\frac{\xi}{R_o}\right)^4 F\left(\frac{2BR_o}{\xi}\right) e^{2BR_o/\xi} \tag{4-3}$$

where A=0.45, B=1.39, D≃1, F(x) is equal to one for large x, ξ is the three dimensionally averaged decay length, and R_o is the minimum hopping distance. For variable range hopping,

$$\frac{\sigma(\infty)}{\sigma(0)} = \frac{3\pi(2.3)}{0.2}\left(\frac{T}{T_o}\right)^{3/2} G \exp\left[+\left(\frac{T_o}{T}\right)^{1/4}\right] \tag{4-4}$$

where G≃1 and T_o is defined by the DC conductivity of variable range hopping model:

$$\sigma(\omega=0) = 0.2e^2\Gamma_o\rho_o\ \xi^2\left(\frac{T_o}{T}\right)^{1/2} \exp\left[-\left(\frac{T_o}{T}\right)^{1/4}\right] \tag{4-5}$$

So T_o can be calculated from the slope of the $\ln(\sigma_{DC})$ vs $T^{-1/4}$ curve. These curves are plotted in Fig.4-13 and Fig.4-14 for the y=0.02 sample with z=0 and z=0.0006, and in Fig.4-15 and Fig.4-16 for y=0.17 sample with z=0 and z=0.0005. The calculated T_o for each sample is listed in table 4-1. The predicted $\sigma(\omega)/\sigma(0)$ ratio by Eq.4-4 and Eq.4-5 compared with the expermental values are also listed in table 4-1. The experimental values of $\sigma(\omega)$ used here were obtained from the optical conductivity which will be discussed later. ξ=3.6Å is the value used by Kivelson. R_o was calculated by

$$R_o = [(4\pi/3)\ C_{im}]^{-1/3} \tag{4-6}$$

where $C_{im}=\rho Z$ is the impurity concentration in cm^{-3} and $\rho=5.22\ 10^{22} cm^{-3}$ is the density of CH units. For the undoped sample, Kivelson[12] proposed an "accidental" doping level with z=0.0002. This corresponds to $C_{im}=1.3\ 10^{19} cm^{-3}$ and R_o=26.7 Å(this R_o was used for all undoped samples). For z=0.0005 doped samples, R_o=20.5 was used. From table 4-1, one can see that the undoped y=0.17 samples are in better agreement with variable range hopping, while those for y=0.02 and doped y=0.17 fit more closely the isoenergetic hopping model. But the hopping distance R_c is longer than R_o, which is the hopping distance for ordinary $[CH]_x$ with the same doping level.

Optical Properties of Segmented Polyacetylene

Using the Perkin-Elmer monochromator spectrometer described in Chapter III, the absorption coefficient of $[CHD_y(I_3)_z]_x$ in the 700 to 5000 cm^{-1} frequency range was obtained by transmission measurements.

The absorption coefficient, α, is defined as

$$\alpha = -(\frac{1}{d}) \ln(T) + (\frac{2}{d})\ln(1-R) \qquad (4\text{-}7)$$

where "d" is the thickness of the sample, "T" is the transmitance and "R" is the reflectance. Since "R" is less than 2% in this frequency range for all of these $[CHD_y(I_3)_z]_x$ samples, the absorption coefficient is approximately determined by

$$\alpha = -(\frac{1}{d})\ln(T) \qquad (4\text{-}8)$$

The results for y=0.02 and y=0.17 are plotted in Fig.4-17 and Fig.4-18 respectively.

It is a general feature of doped polyacetylene that vibrational modes at 880 cm^{-1}, 1290 cm^{-1} and 1400 cm^{-1} are strongly enhanced by doping. This enhancement has been observed in all doped polyacetylene samples with dopant materials as varied as iodine, AsF_5, ClO_4, and Na. Mele and Rice [43] pointed out that 1290 cm^{-1} and 1400 cm^{-1} are associated with internal vibrations of charged solitons, whereas the broad maximum occurring between 500 and 900 cm^{-1} is the pinning mode of the soliton according to Horovitz [53,54]. These modes are thus very important for investigating the relationship between the charged soliton population and conjugation length. The assignment of the observed vibrational modes in conventional polyacetylene by Will et al.[67] are listed in table 4-2.

That the 1400 cm^{-1} mode is not observed in undoped samples of y=0.02 and y=0.17 indicates that the compensation after Na doping was complete. The strong peak at 740 cm^{-1} in Fig.4-17 shows that there is a residual amount of cis-$[CH]_x$ in the y=0.02 sample. In contrast,for y=0.17 sample as shown in Fig.4-18, this mode (as well as 1118 cm^{-1}, 1247 cm^{-1}, 1329 cm^{-1} modes related to cis-$[CH]_x$ in table 4-2) is reduced to zero, showing that the cis-trans isomerization was completed by the heavy sodium doping. This assures us that the cis-like conducting pattern in the y=0.17 undoped sample is not due to residual cis-$[CH]_x$. From Fig.4-17, one can see that y=0.02 samples showed the strong enhancement at 880 cm^{-1}, 1290 cm^{-1} and 1400 cm^{-1} modes with dopant level as low as 0.03%. The oscillator strength of these models grows in proportion to the dopant level as it does in ordinary trans-$[CH]_x$. In contrast, Fig.4-18 showed this enhancement starts at higher dopant level (0.05%) for the y=0.17 sample.

An in-situ optical and conductivity measurement of the y=0.16 sample during I_2 vapor phase doping was also carried out using the apparatus sketched in Fig.4-19. Transmission in the range of 700 cm^{-1} to 5000 cm^{-1} was measured for several different dopant level. The absorption coefficient spectrum obtained by transmission measurement is plotted in Fig.4-20. From Fig.4-17, Fig.4-18 and Fig.4-20, one can see the oscillator strength of 890 and 1400 cm^{-1} mode increases when the dopant level z increases.

Since the index of refraction, "n", is almost a constant of frequency for polyacelylene with low doping level, the partial conductivity sum rule [68] can be written as

$$N_{eff} \frac{m_e}{m^*} = \frac{m_e n c^2}{\pi N e^2} \int_{\omega_1}^{\omega_2} \alpha(\omega)\, d\omega \tag{4-8}$$

where "c" is the speed of light, m_e is electron mass, "N" is the density of CH units, and N_{eff} is the density of effective charge carriers with effective mass m^*. The index of refraction "n" can be calculated from the reflectance measurement. The interference of light multiply reflected between the front and back surface of the film causes a periodic oscillation in the reflectance. The period of these oscillations is related to the refractive index, n, of the film by

$$n = \frac{1}{2d\Delta\omega} \tag{4-9}$$

where $\Delta\omega$ is the frequency spacing of the maxima (or minima) of the oscillations and "d" is the thickness of the film. From Eq.4-9, $n \simeq 1.66$ is obtained with $d=0.01\ cm^{-1}$ and $\Delta\omega=30\ cm^{-1}$. Using $\rho=0.4 g/cm^3$ for polyacetylene, we get $N=1.85\times10^{22}\ cm^{-3}$. By substituting these values and the integrated oscillator strength of 1400 cm^{-1} mode into Eq.4-8, the values of $N_{eff}(m_e/m^*)$ corresponding to this mode for the $[CHD_y(I_3)_z]_x$ sample with $y=0.16$ is calculated and plotted in Fig.4-21. The results from reference 69 for ordinary $[CH]_x$ is also plotted in Fig.4-21. From Fig.4-21, one can see the $N_{eff}(m_e/m^*)$ for the $[CHD_y(I_3)_z]_x$ sample with $y=0.16$ reduced to about 1/6 of the value for ordinary $[CH]_x$ at the same doping level. This reduction can be viewed as either the population of charged solitons per dopant ion is reduced to 1/6 or the effective mass of the soliton is increased due to the short conjugation length effect.

The dopant concentration of $z=0.016$ and $z=0.026$ were determined by weight uptake; other values of "z" were estimated from the conductivity vs dopant level curve in Fig.22. This curve has the same functional form as that for conventional trans-$[CH]_x$ which is also plotted in Fig.4-22 [69], except that the magnitude was reduced by a factor of 10^{-4}.

It was not possible to achieve the I_3 dopant level in the $y=0.16$ sample as high as in ordinary $[CH]_x$. The highest level we reached (by keeping the sample in contact with iodine crystals in an evacuated vessel for 12 hours) was z=0.026, compared to y=0.067 in $[CH(I_3)_y]_x$.

The isoenergetic hopping feature together with the absorption modes at 880 cm^{-1}, 1295 cm^{-1} and 1400 cm^{-1} for the doped y=0.17 sample is a clear evidence of the existence of charged solitons in this sample. For y=0.17, the average conjugation length "L" is only 6 CH units long, whereas the soliton length, 2ξ, is believed to be as long as 14 CH units. Since the doping induced charged soliton still can be formed in y=0.17 samples, there must be some percentage of long conjugation length pieces remaining. Optical measurements of the Peierls gap support this idea. Bredas et al.[70] calculated that the Peierls energy gap increases with decreasing chain length. The calculated results are given in table 4-3.

At high frequencies (greater than 5000 cm^{-1}), all $[CHD_y(I_3)_z]_x$ samples become so highly absorbing that transmission measurements could not be made. Instead, the reflectance of these samples was measured. The absolute reflectance was determined by measuring the reflectance of the sample and normalizing that by the reflectance of the same sample with a 2000 Å gold coating. This normalization procedure allowed for corrections due to surface scattering and the irregular shapes of the samples.

The other optical functions were calculated from the Kramers-Kronig analysis [68] of the reflectance. The details of the Kramers-Kronig transform will be given in the Appendix. The absorption coefficient between 5000 cm^{-1} and 25000 cm^{-1} is plotted in Fig.4-23. The results are summarized in table 4-4. The peak position shifts to higher frequency as the "y" value increases, showing that the chain length is getting some what shorter with wider band gap. However, the peak position indicates that the assumed L=1/y relation is not correct. Instead of L=6 derived from L=1/y for the y=0.17 sample, L=30 was estimated by using table 4-3. The reduction in peak height shows that the number of segments with L>30 reduced to about 50% of the y=0.02 sample and about 1/3 of the ordinary $[CH]_x$. The inconsistency between the L=1/y assumption and the band gap can be interpreted by the "bimodal distribution of conjugation length" theory proposed by Mulazzi et al.[71]. According to this theory, there are two peaks in the conjugation length distribution instead of only one as in normal or Poisson distribution. The conjugation length at which the second peak of the distribution is located might be so short (L<6) that the interband transition is located beyond the high frequency limit (25000 cm^{-1}) of our measurements. Using Mulazzi´s bimodal distribution theory, Lefrant calculated the conjugation length distribution from resonant Raman scattering data. The result is shown in Fig.4-24, it is in agreement with our optical data.

In summary, the segmented polyacetylene--$[CHD_y(I_3)_z]_x$ showed similarities in electronic and optical properties to ordinary polyacetylene--$[CH]_x$. The temperature and frequency dependent conductivity is in good agreement with inter-soliton isoengergetic hopping model. The enhancement of doping induced vibrational modes at 880 cm^{-1}, 1290 cm^{-1} and 1400 cm^{-1} indicates charged soliton formation upon doping. But several interesting differences are also observed. The optical interband transitions provide some indication of the proposed bimodal distribution of conjugation length, as well as the variation of this distribution with changing y value. For the $y=0.17$ undoped sample, the temperature and frequency dependent conductivity fits the Mott type variable range hopping model and the oscillator strength of 1400 cm^{-1} mode was decreased with increased y value at the same doping level; the hopping distance was increased with increased y value. All of these can be interpreted as due to a reduction in population or increased effective mass of charged soliton by the short conjugation length.

Heavily Doped Polyacetylene

Sample Preparation

This section will focus on the results from perchlorate doped polyacetylene. The samples were prepared using the Shirakawa technique and doped electrochemically by the research group at the Xerox Webster Research Center. The 80 to 100 microns thick free standing films have fibrillar morphology consisting of matted fibrils with 200 to 300Å diameter. The as-grown cis-$[CH]_x$ was isomerized to trans-$[CH]_x$ by heating in an inert atmosphere at $180^{\circ}C$ for 2 hours. The electrochemical doping was carried out by a method similar to that described in reference 72. The samples were doped with ClO_4^- ions from a $LiClO_4$ solution in acetonitrile using Pt as a counter electrode. Concentrations were determined by weight uptake. Each doped film was cut up and portions were distributed for different measurements.

Magnetic Susceptibility and Electric Conductivity.

Magnetic susceptibility was measured with a high-field Faraday balance. Four-probe electrical conductivity and thermopower measurements were done simultaneously in a closedcycle refrigerator. All of these measurements were done by Epstein et al.[73]. (Since the optical properties were measured from the same samples, these magnetic and electronic properties should be discussed here too).

The effect of doping on the room-temperature conductivity and on the Pauli susceptibility X^{PAULI} is shown in Fig.4-25. X^{PAULi} is directly proportional to the Fermi-energy density of states, $N(E_F)$. The susceptibility has been normalized by $X^{METAL}=\mu_B^2N_o$, where X^{METAL} is the susceptibility of "metallic" $[CH]_x$ in the absence of a Coulomb repulsion and N_o is the expected value of $N(E_F)$ for "metallic" polyacetylene. N_o was estimated by assuming a half filled, one-dimensional, tight-binding band of width W=10eV, for which $N_o=4/W=0.13$ states/(eV-C_{atom}). Three regions may be identified in these data. Region I with $0<z<0.02$ has low values of both conductivity and $N(E_F)$. The electronic structure in this light doping regime is that of semiconducting $[CH]_x$ with relatively isolated charged solitons induced by doping, although band tailing due to disorder is important. In region II, where $0.02<z<0.04$, the conductivity is quite high yet $N(E_F)$ is low. Region III, with $0.04<z<0.08$ is one of the principal subject of this study. Here both conductivity and $N(E_F)$ are high, although $N(E_F)$ reaches only about 80% of the value expected for metallic $[CH]_x$.

Epstein et al.[73] also measured the temperature dependent susceptibility of samples doped in these three regions and derived the density of states as shown in Fig.4-26. The schematic electron band structure is shown in Fig.4-27. The full gap (valence to conduction band) is 2Δ, the gap between the valence band and soliton band is 2δ. The Fermi energy for acceptors lies between the valence and soliton bands. Disorder leads to a finite density of localized states in the gap 2δ. The density of states in the vicinity of E_F can then be expanded in powers of E (defining $E_F=0$) as $N(E)=No+N_1E+(1/2)N_2E^2$ (where $N_1=0$). Then the Pauli susceptibility is $X^{PAULI}=2\mu_B^2[No+(\pi^2/6)(K_BT)^2N_2)$. The Mott type variable range hopping model for constant N(E) introduced in chapter II has been modified [33] to include this varying N(E). Epstein et al.[73] found that the conductivity and magnetic susceptibility data for y=0.01 to y=0.05 $[CH(ClO_4)_y]_x$ agrees with this generalized variable range hopping theory very well.

Optical Properties of Heavily Doped Polyacetylene

Using the Michelson interferometer and the PE spectrumeter, the reflectance of y=0.16 to y=13.5 $[CH(ClO_4)_y]_x$ samples were measured through 50 cm^{-1} to 25000 cm^{-1} frequency range. Using the Kramers-Kronig transform, the optical conductivity was obtained.

This quantity is plotted in Fig.4-28 with region I represented by $z=0.016$, region II by $z=0.035$, and region III by $z=0.061$. The characteristic modes of the charged soliton at 800 cm^{-1} 1290 cm^{-1} and 1400 cm^{-1} exist at all doping levels. Even at extremely high doping level ($z=0.13$), this feature still remains in the spectrum. But the quite different spectra taken from different portions of the same sample indicates that the degradation starts when the doping level exceeds 8%. Fig.4-29 shows the conductivity divided by the doping levels over the 700 cm^{-1} to 5000 cm^{-1} frequency range. It shows that the oscillator strength of the 1290 cm^{-1} and 1400 cm^{-1} modes is proportional to the doping level up to $y=0.06$. This means that the "one dopant ion creates one charged soliton" result of Epstein et al.[36] is still valid in the heavily doped region (region III). Since charged solitons remain in the extremely highly doped sample, the bond alternation is not suppressed by heavy doping and the Peierls-gap is not closed for heavily doped polyacetylene. Thus the Peierls gap closing model must be ruled out. From Fig.4-28, one can see the optical transition between the valence band and conduction band of the undoped polymer, which occurs at 2 =11000 cm^{-1} (1.4eV), is seen as the dominant feature in region I. It is weaker in region II. And it is essentially not observed in region III. This transition is absent in all of the samples with $y > 0.045$. The doping related midgap absorption is a shoulder at 6000 cm^{-1} (0.75eV) in region I samples. In region II, the strength of this absorption increases and the center frequency is lower. Finally, in region III, there is a peak at 4000-5000 cm^{-1} (0.5-0.6eV), which is the only strong electronic absorption in the entire frequency region below 25000 cm^{-1}.

Fig.4-30 shows the optical conductivity of a partially oriented sample with doping level in region III, prepared by stretching a piece of undoped $[CH]_x$ to approximately 1.8 times its original length and then doping it. The interband transition at 2 =1.4eV is observed in neither polarization. Instead, there is a single peak, which is seen to be much stronger for polarization along the polymer chain (i.e., the stretching direction), with an onset at 1500 cm^{-1} (0.2eV) and a maximum at 3000 cm^{-1} (0.4eV). Note that this peak is at a substantially lower energy than "midgap" absorption, which occurs at 6000 cm^{-1} (0.7eV) in region I samples. The low frequency vibrational modes are also stronger for polarization along the chain-axis. The only good explaination for the disappearance of the primary interband transition at 1.4eV in existing theories is the incommensurate state theory. Calculations by Jestin et al.[74] suggested that the primary 1.4eV interband excitation is absent in the incommensurate case because, not being a direct vertical excitation (in an extended zone scheme), it is not allowed. Based on this argument as well as the high conductivity and susceptibility of Fig.4-25, we proposed that heavily-doped polyacetylene is best described as a gapless incommensurate Peierls insulator [17]. According to this model, the bond alternation or charged density wave which causes the gap in the first place still exists at high doping levels but is incommensurate with the lattice. This Peierls distortion ordinarily would render the polymer an insulator but in the case of strong disorder the gapless state exists with a finite but reduced Fermi-surface density of states and DC conductivity. The gapless Peierls state is analogous to the gapless state in superconductors, except that in the latter case it is induced by scattering from magnetic impurities whereas in the former it results from ordinary impurity scattering.

The rapidity of the "transition" to the gapless state as a function of concentration may be understood in terms of the relative suddenness of the onset of severe disordering of the CDW as its charge begins significantly to delocallize from soliton centers. This onset occurs approximately at concentrations for which soliton overlap begins, or more quantitatively, at the concentration $C^* = (E_s/W)$, or $C^* = 0.045$ for a bandwidth $W = 10eV$ and a soliton energy $Es = 0.45eV$. The point is that the dopant ions can not significantly disorder the Peierls system until the charge donated to it or removed from it (by the dopant) has delocalized; as soon as the latter occurs the disorder is severe. The important role of disorder in this incommensurate-commensurate CDW transition could be seen in Fig.4-31, in which the optical conductivity of iodine doped $[CH]_x$ and $[CHD_y]_x$ were plotted Vs frequency. The interband transition at 1.4eV remains the dominant absorpton over the midgap transition with dopant level as high as 3.3% in $[CH(I_3)_z]_x$ but with greatly reduced intensity and the midgap transition becomes the dominant absorption at 2.6% doping level in highly disordered system $[CHD_y(I_3)_z]_x$.

In summary, at high doping concentration, polyacetylene undergoes a transformation into a state characterized by high DC conductivity, by a large Pauli susceptibility and by the absence of the interband transition of the undoped polymer. The IR spectrum shows a pseudo-gap at 0.2 ev and vibrational modes which imply that the carbon-carbon bondlength alternation is not suppressed by heavy doping. This state is best described as a gapless incommensurate Peierls insulator.

Table 4-1

Conductivity Parameters of two hopping model

Sample		T_o		R_o	$[\sigma(\infty)/\sigma(0)]_{ISO}$	$[\sigma(\infty)/\sigma(0)]_{VHR}$	$[\sigma(\infty)/\sigma(0)]_{EXP}$	R_C*
$[CHD_y(I_3)_z]_x$		10^8K				(From T=300K)		
y	Z							
0	0 #	19	3.6	26.7	6×10^4	4×10^{13}	1.3×10^4	24.2
0	0.05 #	0.01	3.6	4.42	2.67	1	1	4.42
0.02	0	20	3.6	26.7	6×10^4	4×10^{13}	1×10^8	30
0.02	0.0005	16	3.6	20.51	1.4×10^3	6.5×10^{12}	1×10^4	25
0.17	0	6	3.6	26.7	6×10^4	2.34×10^9	1×10^{10}	\
0.17	0.0005	24	3.6	20.51	1.4×10^3	6×10^{14}	5×10^4	26.7

*. Using the experimental $[\sigma(\infty)/\sigma(0)]_{EXP}$ as input, R_c is the calculated hopping distance of isoenergetic model.

#. From reference 33.

Table 4-2

Transmission IR spectra of undoped polyacetylene film.

Frequency (cm^{-1})	Intensity	Assignment
3057	W	C-H stretch in cis-[CH]x
3044	M	C-H stretch in cis-[CH]x
3010	M	C-H stretch in trans-[CH]x
1923	W	C=C=C stretch in allene groupings
1801	S	1329+446 cis-[CH]x
1690	W	1249+446 cis-[CH]x
1483	W	C-H deformation in allene groupings
1376	W	C=H stretch, dopant activated
1329	S	C-H in plane bend in cis-[CH]x
1294	W	C-H in plane bend in trans-[CH]x
1247	M	C-H in plane bend in cis-[CH]x
1118	M	C-C atretch in cis-[CH]x
1018	VS	C-H out of plane bend in trans-[CH]x
888	W	C-H in-plane bend, dopant-activated
740	VS	C-H out of plane bend in cis-[CH]x
450	VS	C-C-C bend in cis-[CH]x

VS=very strong, S=strong, M=medium, W=weak, VW=very weak,

From rsference 67

Table 4-3

Energy Gap as a Function of Chain Length for Polyacethlene

Chain length (CH Unit)	energy gap (eV)
1	7.85
2	5.29
3	4.09
4	3.42
6	2.70
10	2.11
∞	1.45

Table 4-4

Interband Transition Peak and Energy Gap for $[CHD_y(I_3)_z]_x$

Y	max	E_g(eV)	L
0.0	11290	1.4	∞
0.02	12000	1.49	60
0.17	14500	1.78	30

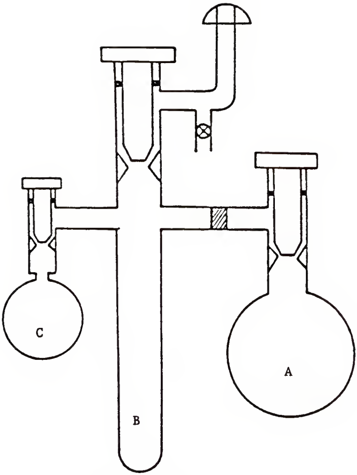

A Compensating alcohol (CH_3CH_2OD or CH_3OD)

B Sodium naphthalide solution

C Sample bulb

Figure 4-1
Schematic diagram of apparatus for preparing segmented $[CH]_x$.

From reference 61

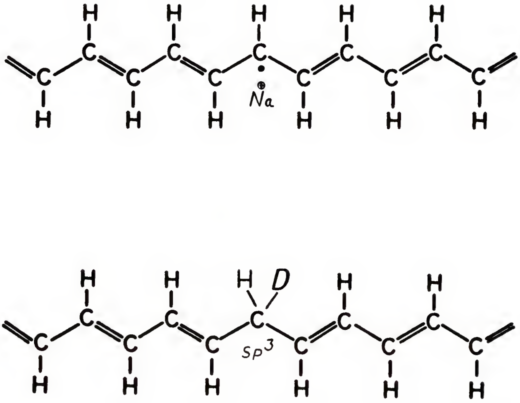

Figure 4-2
Schematic diagram of introducing sp^3 defects on $[CH]_x$ chain.

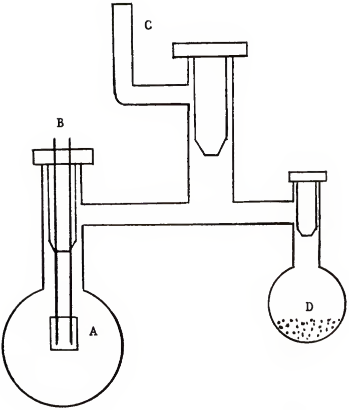

A Sample
B Conductivity measurement probe
C Pumping line
D Iodine

Figure 4-3
Schematic diagram of apparatus for doping $[CHD_y]_x$ sample by I_2 vapor.

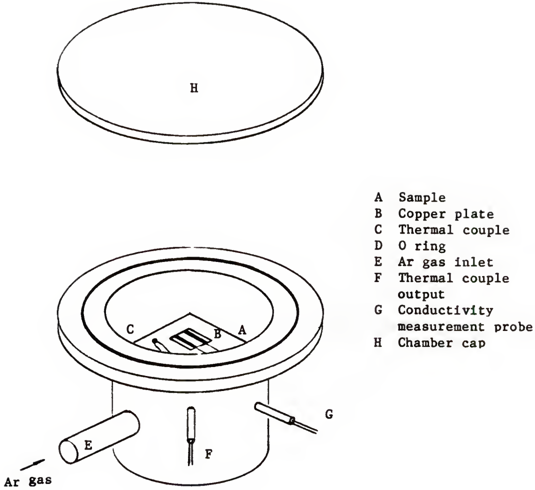

Figure 4-4
Schematic diagram of sample chamber for conductivity measurement.

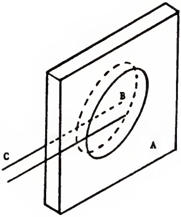

(a)

Sandwich type cell

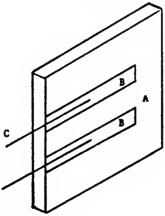

(b)

Stripe type cell

Figure 4-5
Schematic diagram of sample cell for conductivity measurement.

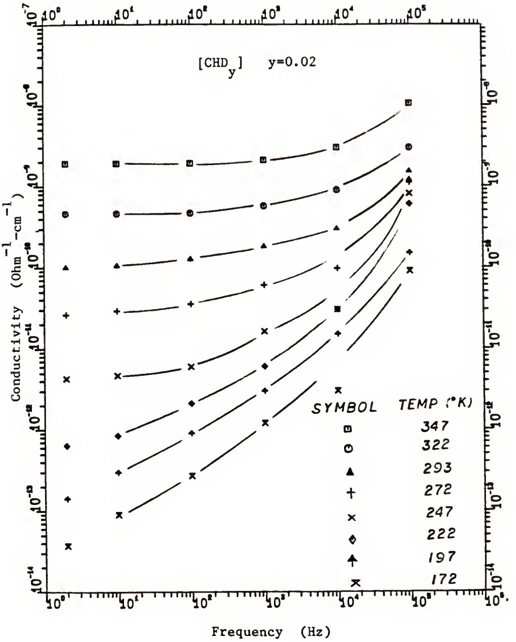

Figure 4-6
Temperature and frequency dependent conductivity of $[CHD_y]_x$ with y=0.02.

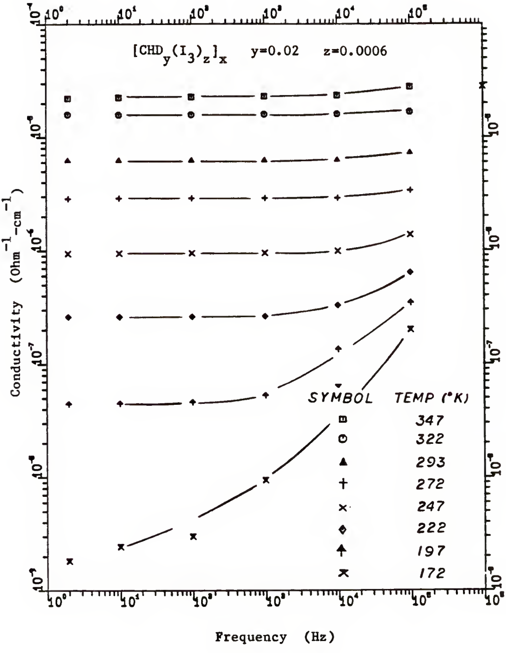

Figure 4-7
Temperature and frequency dependent conductivity of $[CHD_y(I_3)_z]_x$ with y=0.02 z=0.006.

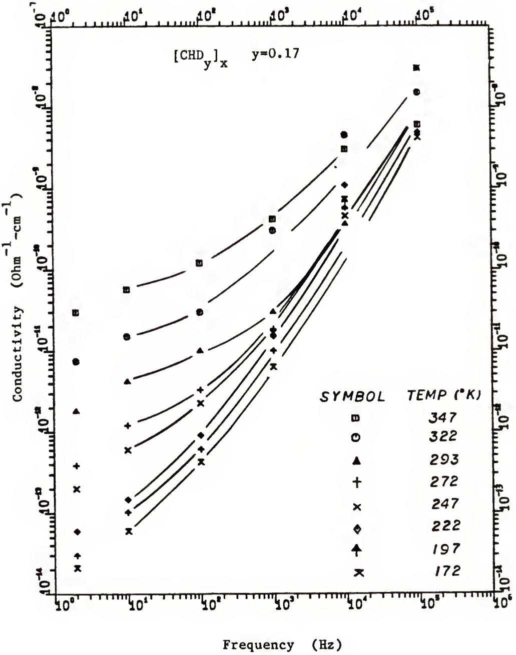

Figure 4-8
Temperature and frequency dependent conductivity of $[CHD_y]_x$ with y=0.17.

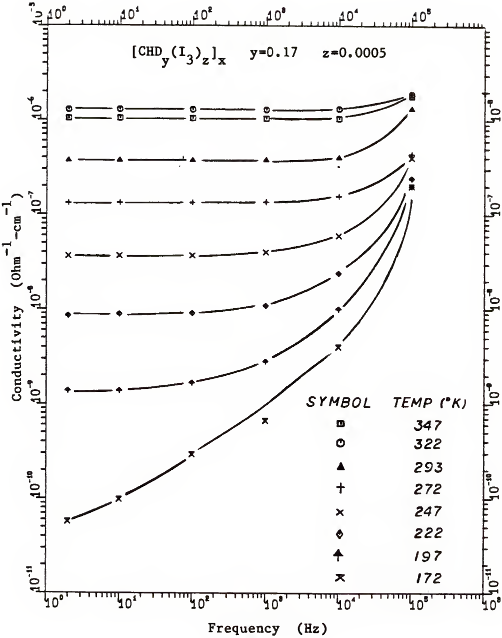

Figure 4-9
Temperature and frequency dependent conductivity of $[CHD_y(I_3)_z]_x$ with y=0.17 z=0.005.

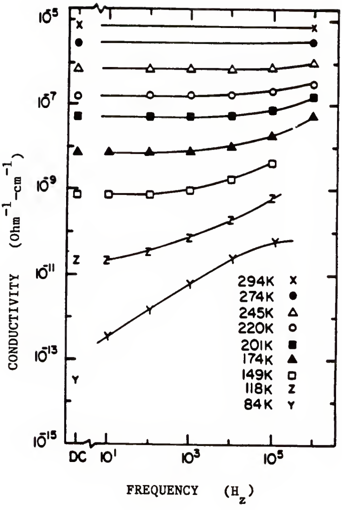

Figure 4-10
Temperature and frequency dependent conductivity of ordinary trans-$[CH]_x$.

From reference 65

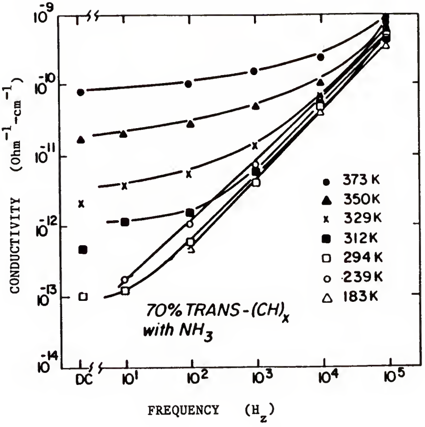

Figure 4-11
Temperature and frequency dependent conductivity of ammonia compensated-[CH]$_x$.

From reference 65

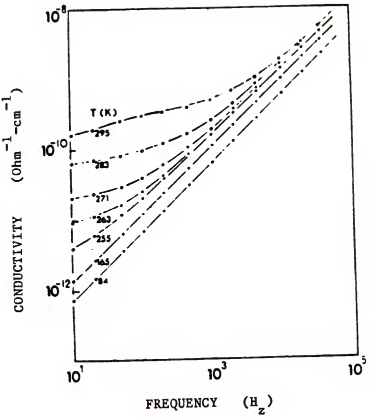

Figure 4-12
Temperature and frequency dependent conductivity of amorphous silicon.

From reference 66

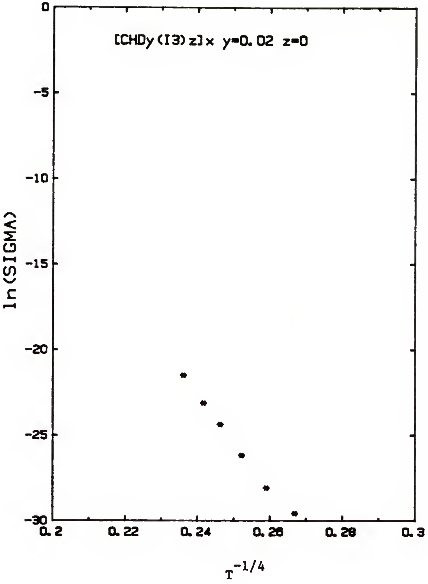

Figure 4-13

DC conductivity versus $T^{-1/4}$ for $[CHD_y(I_3)_z]_x$ with y=0.02 z=0.

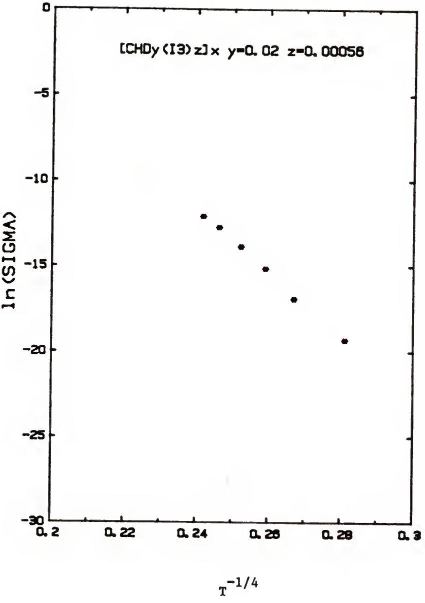

Figure 4-14

DC conductivity versus $T^{-1/4}$ for $[CHD_y(I_3)_z]_x$ with y=0.02 z=0.0005.

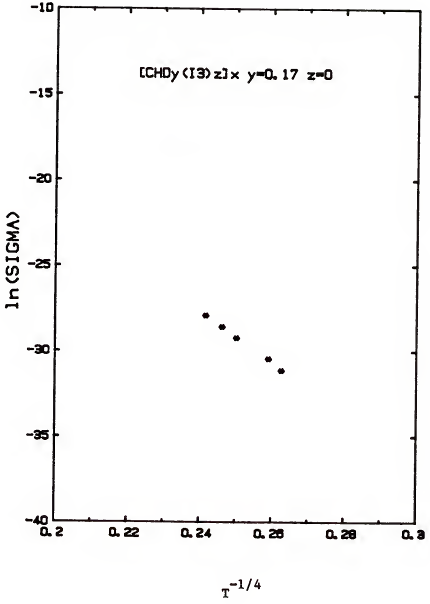

Figure 4-15

DC conductivity versus $T^{-1/4}$ for $[CHD_y(I_3)_z]_x$ with y=0.17 z=0.

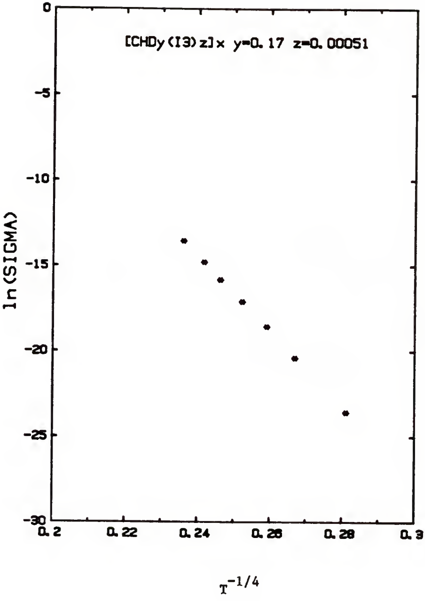

Figure 4-16

DC conductivity versus $T^{-1/4}$ for $[CHD_y(I_3)_z]_x$ with y=0.17 z=0.0005.

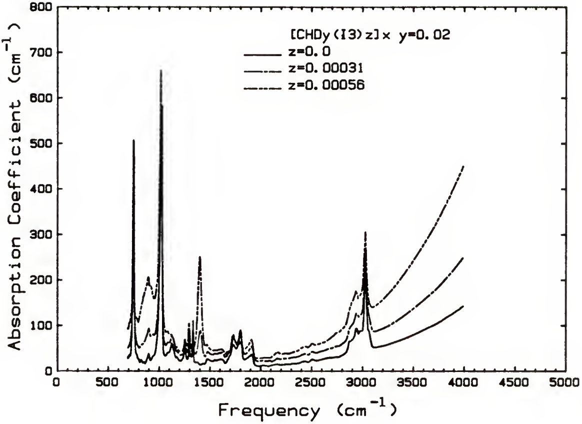

Figure 4-17
IR absorption coefficient of $[CHD_y(I_3)_z]_x$ samples
with y=0.02, z=0 z=0.0003 and z=0.0006.

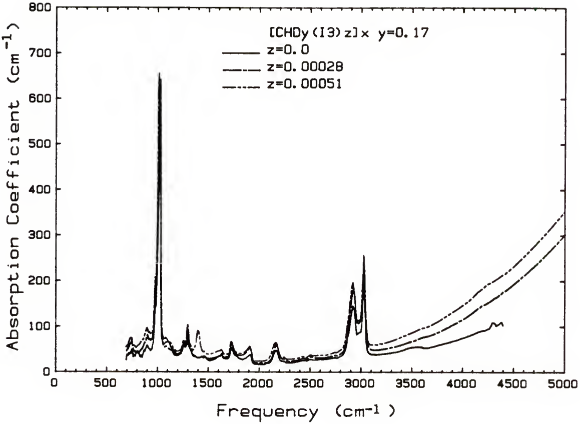

Figure 4-18
IR absorption coefficient of $[CHD_y(I_3)_z]_x$ samples

with y=0.17, z=0 z=0.0002 and z=0.0005.

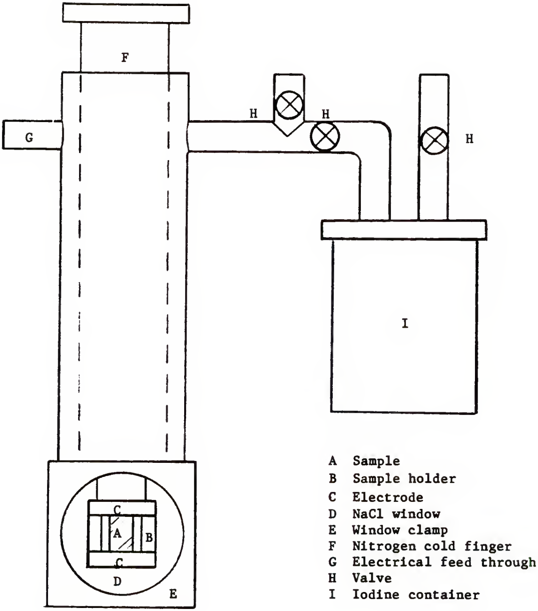

A	Sample
B	Sample holder
C	Electrode
D	NaCl window
E	Window clamp
F	Nitrogen cold finger
G	Electrical feed through
H	Valve
I	Iodine container

Figure 4-19
Schematic diagram of apparatus for in-situ optical and conductivity measurement during iodine vapor doping.

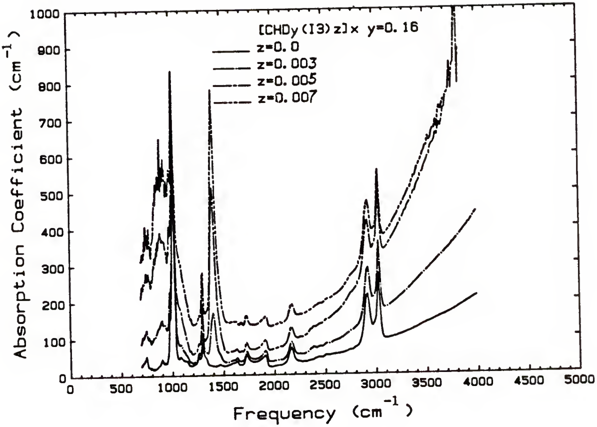

Figure 4-20
IR absorption coefficient of $[CHD_y(I_3)_z]_x$ samples

with y=0.16 z=0 z=0.003 z=0.005 and z=0.0007.

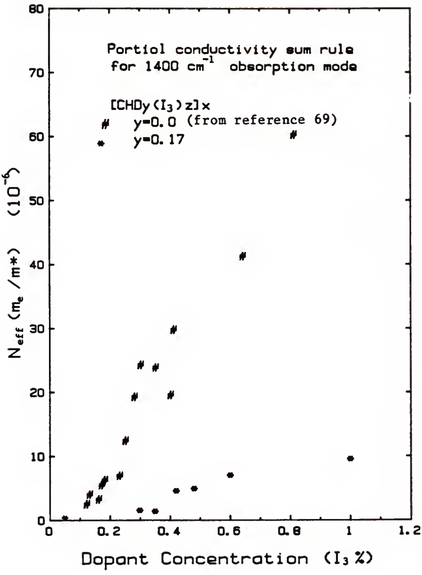

Figure 4-21

Partial conductivity sum rule for 1370 cm^{-1} absorption mode in $[CHD_y(I_3)_z]_x$ samples with y=0 and y=0.16.

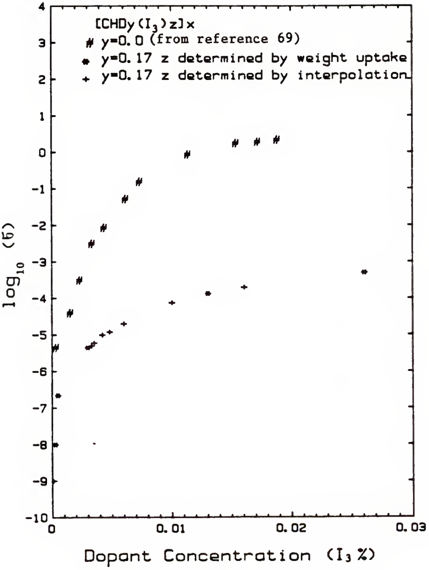

Figure 4-22
Conductivity as a function of dopant level of $[CHD_y(I_3)_z]_x$ samples with y=0 and y=0.16.

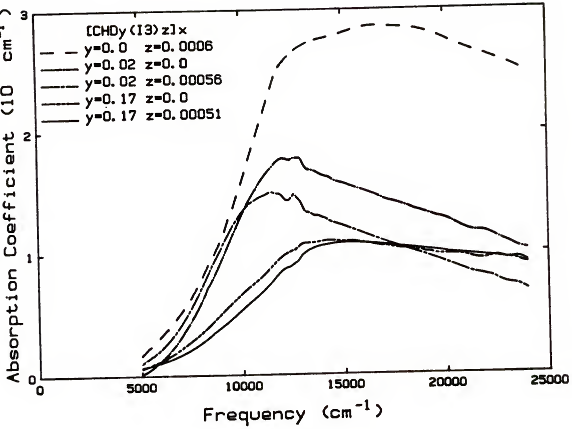

Figure 4-23
Absorption coefficient in the interband transition frequency range for $[CHD_y(I_3)_z]_x$ sampls with y=0 y=0.02 and y=0.17.

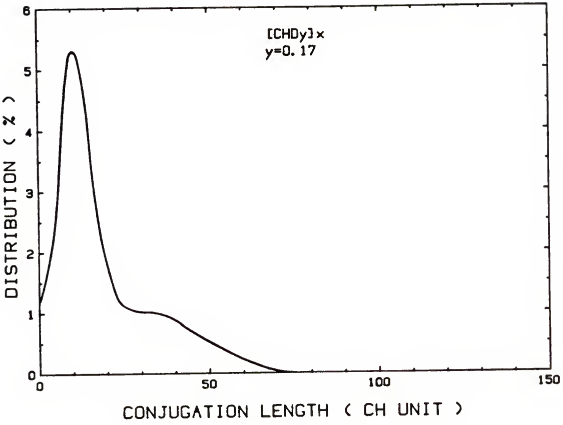

Figure 4-24
Bimodel distribution of conjugation lengths obtained by fitting the Raman scatlering data to the "Mullazi theory".

Calculated by Lefrant

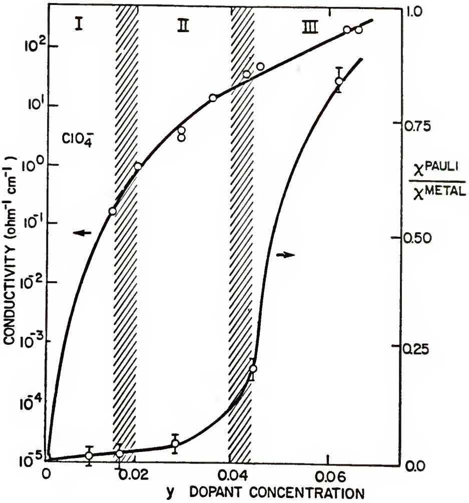

Figure 4-25
Room temperature DC conductivity (left hand scale) and magnetic susceptibility (right hand scale) versus dopant concentration.

From reference 72

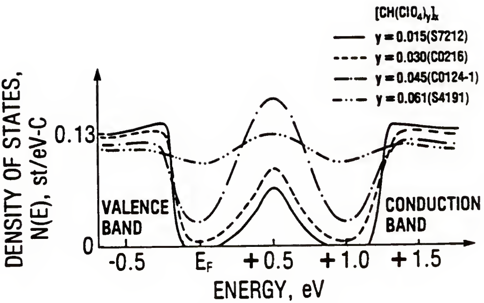

Figure 4-26
Schematic diagram of electronic stracture
of $[CH(ClO_4)_y]_x$ derived from X^{Pauli}.
From reference 72

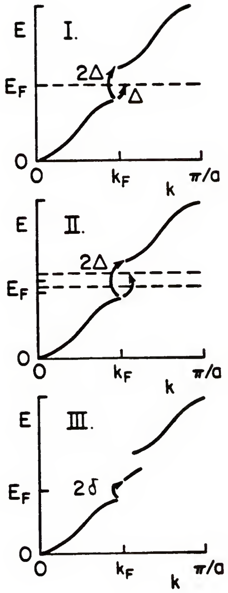

Figure 4-27
Schematic representation of the energy-band structure

From reference 72

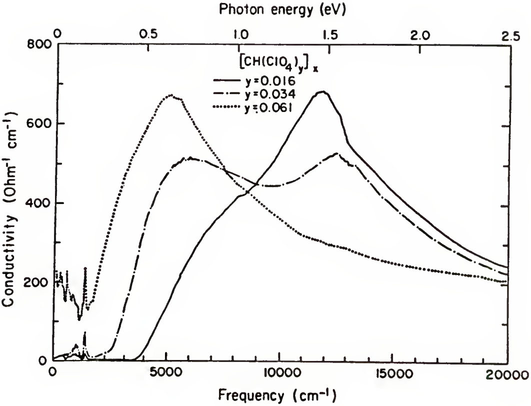

Figure 4-28
Frequency dependent conductivity of perchlorate-doped $[CH]_x$.

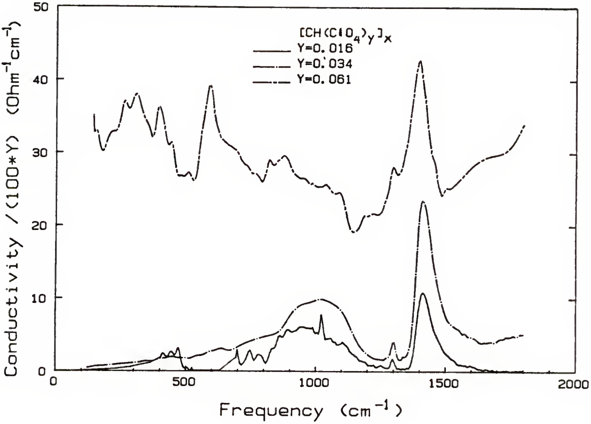

Figure 4-29
Ratio of frequency-dependent conductivity to dopant concentration.

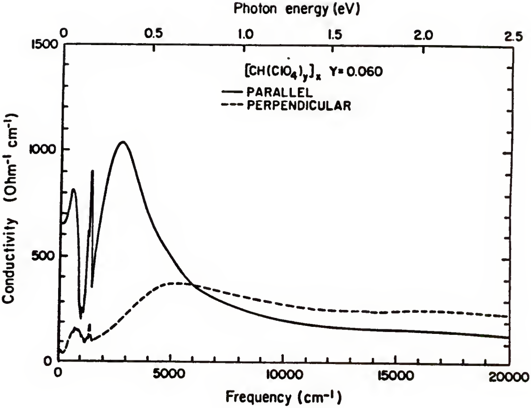

Figure 4-30
Frequency dependent conductivity of stretch-oriented heavily-doped $[CH]_x$.

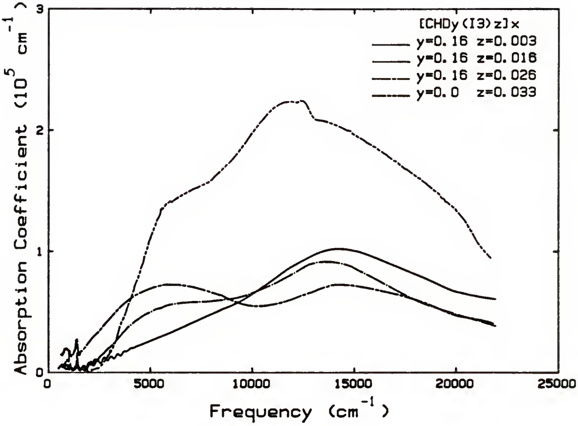

Figure 4-31
Absorption coefficient in the interband transition frequency range for $[CHD_y(I_3)_z]_x$ with y=0.16.

CHAPTER V
DISCUSSION AND CONCLUSIONS

Segmented Polyacetylene and Soliton

The charge transport and optical properties of segmented polyacetylene described in last chapter provide a great deal of interesting information about polyacetylene.

Charged Soliton and Conjugation Length.

With the average conjugation length as short as 6 ($y=0.16$), optical properties of doped segmented polyacetylene, $[CHD_y(I_3)_y]_x$, showed the same features as conventional $[CH(I_3)_y]_x$: The oscillator strength of the vibrational modes related to charged solitons at 880 cm^{-1}, 1290 cm^{-1} and 1400 cm^{-1} increases as doping level increases; the optical transition related to the midgap charged soliton state starts at 6000 cm^{-1} (0.7ev) with low doping level and grows and shifts to lower frequency as doping level increases; and the interband transition across the Peierls gap at 11000 cm^{-1} (1.4eV) reduces its oscillator strength upon doping and finally disappears at high doping level ($z=0.026$). So, the charged soliton is created upon doping in the same manner as conventional polyacetylene. However, the population of charged solitons derived from the oscillator strength of 1400 cm^{-1} mode was reduced to about 1/6 of the ordinary polyacetylene for y=0.16 $[CHD_y(I_3)_z]_x$ sample. Since charged soliton can only be created on the long conjugation length segments, the reduction of charged soliton population indicates the reduction of long chain segments. It is a natural result of high concentration of sp^3 defects.

However, if the average conjugation length L=1/y, is assumed to be 6a, the probability of creating one charged soliton by each dopant ion should be almost zero (soliton length 2 =14a). But the interband optical transition in Fig.4-23 shows a significant fraction of long chain segments. Thus the assumption of a relation between conjugation length L and concentration value y of L=1/y should be reconsidered. Because the sp^3 defect is introduced by converting a charged soliton into a sp^3 CHD group, the concentration of sp^3 defects, depends on the concentration of charged solitons created by sodium doping. When the doping level is as high as 16%, it is possible that not all the sodium dopant will be able to transfer charge to the $[CH]_x$ chain. So the concentration of sp^3 defects would be lower than the sodium concentration at high sodium doping level. An alternate possibility is that the distribution of charged solitons is extremely nonuniform leading to a bimodal distribution of conjugation lengths. So, whether there are preferential positions along the $[CH]_x$ chain or preferential chains for forming charged solitons will be a very interesting problem for further investigation. The reduction of oscillation strength of the 1400 cm^{-1} mode can also be viewed as the increasing effective mass of charged soliton. This in turn means the soliton length 2 is reduced. From the energy curve shown in Fig.2-9, forming shorter length solitons is possible at the cost of higher formation energy.

It should also be noticed that the highest achievable doping level is decreased as y increased. This is another evidence of the important role of soliton and other conjugation defects in polyacetylene. It was proposed by some researchers [75] that the high dopability and conductivity of $[CH]_x$ is basically due to the dilute density and spagatti-like morphology which preserved enough space and surface area for absorbing and disabsorbing dopant material. This is not true. The highest achievable doping level for $[CHD_y(I_3)_z]_x$ sample is about 2.6% compared to 6% for ordinary $[CH(I_3)_y]_x$. This indicates the microscopic structure plays an important role: the dopant ion is more stable when the charge transfer takes place by creating charged soliton, as the probability of charged soliton creation reduced due to the high sp^3 defect level, the highest achievable doping level is reduced.

Conductivity and Electron Hopping Among Soliton States.

The charge transport and optical properties of segmented polyacetylene could be better interpreted by the electron hopping among soliton states theory[33]. Two important differences should be mentioned between this theory and the Mott variable range hopping (VRH) theory for amorphous semiconductors: first, the electron only hops among the soliton states, so the hopping rate depends on the intersoliton spacing. Second, $N(E-E_F)$, the density of states in the vicinity of Fermi level, is no longer a constant as assumed in Mott VRH theory, but varies as a function of $E-E_F$,

$$N(E-E_F) = N_o+N_2(E-E_F)^2 \tag{5-1}$$

At very light doping level, the hopping is among the isolated soliton states with the help of mobile neutral soliton. Since the difference between energy levels of isolated soliton states is much smaller than k_BT, Kivelson and Epstein [33] call it isoenergetic hopping. When doping level increases, the interaction between solitons splits the midgap soliton level into a narrow soliton band, and more and more neutral solitons are converted into charged solitons by doping. So the intersoliton hopping is no longer among those states whose energy level difference is within k_BT, but instead among the soliton states in a much wider energy range. Assuming the density of states varies as Eq.5-1, the conductivity calculated by Epstein et al.[73] from the density of states shown in Fig.4-26 argrees very well with experimental results.

Although no quantitative prediction has been made on charge conductivity by the charged soliton diffusion model, one would expect that if the charged soliton difusion were the dominant effect, then the very short chain $[CHD_y(I_3)_z]_x$ sample turn into insulator due to the blockage of soliton diffusion by sp^3 defects. But the conductivity of the y=0.16 and y=0.17 samples do not suport this model. In addition, as shown in Fig.4-22, at each I_3 doping level, the conductivity is reduced by a factor of 10^{-4} as y value changes from 0 to 0.16, while the population of charged solitons (calculated from the oscillator strength of 1400 cm^{-1} mode) is only reduced by a factor of 1/6. This nonlinear relation between conductivity and charged soliton population did not support the soliton liquid model by Dong [15], since the conductivity should be proportional to the number of charge carriers--charged solitons in this model. On the other hand this phenomenon could be explained by the Kivelson-Epstein hopping model. According to Eq.2-63, the DC conductivity exponentially decays as the intersoliton spacing R_o increases. So the DC conductivity decreases with much higher rate than the population of charged soliton.

The frequency and temperature dependence of conductivity of $[CHD_y(I_3)_z]_x$ also agrees with the intersoliton hopping model. The undoped sample of $[CHDy]_x$ with y=0.17 showed a Mott type variable range hopping conductivity like cis-$[CH]_x$. The characteristics of intersoliton hopping, like trans-$[CH]_x$ is recovered by light doping with iodine. The simultaneous appearance of the 1400 cm^{-1} feature linked this conducting mechanism to the population of charged solitons. As introduced in chapter IV, Kivelson [12] assumed a 10^{-4} charged soliton level due to "accidental doping" in his calculation for undoped trans-$[CH]_x$. For y=0.17 sample, all of those charged solitons created by n-type "accidental doping", together with the sodium doping created charged soliton, have been converted into sp^3 defects by the compensation procedure. The probability of creating the charged soliton by any more "accidental doping" reduced to zero after the compensation due to the short conjugation length effect. So the intersoliton isoenergetic hopping feature disappeared and $\sigma(f,T)$ showed all the Mott type hopping feature in the undoped y=0.17 sample. When the charged soliton concentration reached the level of 10^{-4} again by I_3 doping, the isoenergetic hopping among soliton states become the dominant effect again and the trans-like conductivity pattern resumed. But the longer hopping distance reduced the room temperature DC conductivity by a factor of 10^{-4} from the trans-$[CH]_x$ with the same doping level.

Perchlorate Doped Polyacetylene

As a signature of doping induced charged solitons, the vibrational modes at 880 cm^{-1}, 1290 cm^{-1} and 1400 cm^{-1} remains at highest doping concentration. This indicates that polyacetylene in the heighly conducting regime is still a dimerized structure and that the Peierls gap is not closed. Although both the conductivity and $N(E_F)$ are high in the heavily doped ($0.04 < z < 0.08$) regime, but the $N(E_F)$ reaches only about 80% of the value expected for metallic $[CH]_x$. So, the heavily doped $[CH]_x$ is not a metallic state. Based on the conclusion that the Peierls gap has not closed with the disapearence of interband transition at 1.4 eV in Fig. 4-28, heavily-doped polyacetylene is best described as a gapless incommensurate Peierls insulator.

The "soliton glass to soliton liquid" model. Proposed by Dong [15] made no predication about optical features of this transition, so it could not be discussed in detail based on our optical measurement only. But one should keep in mind the one-dimensional and topological feature of soliton in polyacetylene. So the validity of treating this system as a three-dimensional interacting spinless fermion ensemble is questionable.

The "strong Coupling Polaronic Metal" model [14] is a very interesting model. Fesser el al.[25] had calculated the optical obsorption from polarons in a model of polyacetylene. The band diagram of single soliton and single polaron with the possible optical transition is shown in Fig.2-20, the calcalated optical absorption is shown in Fig.2-22, Fig.2-23 and Fig.2-24. Note that the interband transition in these Figures was omited and the unit of frequency is in Δ_o (0,7eV). Although the optical absorption of polaron lattice would have broader peak than single polaron, the new absorption peak due to the optical transiton between two polaron subbands should be observed when the first order phase transition of soliton lattice to polaron lattice took place. And this peak should be located between the midgap transition and interbard transition of the soliton lattice. This absorption was not found in our optical measurement for perchlorate doped polyacetylene. Optical measurement of iodine doped polyacetylene by Tanaka [76] and Epstein et al.[36] sodium doped by Chen [39] did not show this feature either. In addition, since polaron can be viewed as a charged soliton and a neutral anti-soliton pair, converting all the existing charged solitons into polarons requires creating equal number of neutral anti-solitons. This energy barrier to the first-order phase transition needs to be explained in this theory.

In contrast with other models, heavily doped polyacetylene is best described as a gapless incommensurate Peierls insulator. Essentially all of those properties predicted by this model, introduced in chapter II, are observed in heavily doped $[CH]_x$. First, the susceptibility is high but less than the "metallic" value; the reduction of $N(E_F)$ to approximately 0.8 of the metallic value implies the parameter $\eta=1.67$. (Here, $\eta=h/(2\pi\tau\Delta)$ is the Peierls-pair-breaking parameter.) The two strong infrared absorption at 1290 and 1400 cm^{-1} is close to the known Raman frequencies of the undoped polymer [77]. Third, the DC and far-infrared conductivity are reduced to $\sigma_{RT}=150\Omega^{-1}cm^{-1}$ from the Drude metallic value which would approximately correspond to the peak in $\sigma_1(\omega)$ $(\sigma_o=700\Omega^{1}cm^{-1})$, although the reduction is much more than that quantitatively predicted by Rice. $(\sigma=\sigma_o g^2$; if $\eta=1.67$ then $g=(1-\eta^{-2})^{1/2}=0.4$, and $\sigma_{RT}=288\ \Omega^{-1}\ cm^{-1}$.). Fourth, the conductivity increases with increasing T. Thus despite the complexities of actual $[CH]_x$ samples, this model describes heavily doped $[CH]_x$ reasonably well.

The disappearance of the primary interband transition at 1.4eV is evidence that heavily doped $[CH]_x$ has entered a gapless incommensurate Peierls state. The movement to lower energies of a considerable density of one electron levels occasioned by the appearance of the pseudogap at E_F strongly suppresses the 1.4eV interband transition oscillator strength.

The amplitude of the incommensurate lattice distortion, is given by Rice as

$$u = \Delta/2\gamma \sin(k_F a) \tag{5-2}$$

and

$$u = [\Delta_o/2\gamma \sin(k_F a)] \exp[-\phi(\eta)] \tag{5-3}$$

where 2Δ is the incommensurate energy gap, and $2\Delta_o$ denote the incommensurate energy gap in the absence of disorder scattering $(\tau^{-1}\rightarrow 0)$, $\gamma=-\partial t/\partial a(\approx 8\text{eV Å}^{-1})$ is the derivative of the π electron hopping integral with respect to interatomic separation, and

$$\phi(\eta) = \text{arc}\cos(\eta) + \frac{1}{2}(\eta.\text{arc}\sin(\eta^{-1}) - g) \tag{5-4}$$

Using Δ_o=0.25 eV [17] and η=1.67, Eq.5-2 and Eq.5-3 yields Δ=0.1eV, so that $\tau=(\hbar/2\eta\Delta)=4\times 10^{-15}$sec. Then assuming a Fermi velocity of 10^8cm/sec, the mean free path is 40 Å in agreement with the structural coherence length. In contrast, if simple metallic behavior is assumed , the effective DC conductivity would be $\sigma_{RT}=ne^2/3m$, where $m=m_e$ is the effective mass of the conduction electrons, $n=1.7\times10^{22}$ cm^{-3} is their density, and the factor of 3 comes from an orientational average of fibril directions. The measured conductivity of 150Ω^{-1} cm^{-1} then gives $\tau=1\times10^{-16}$ second which gives a 1 Å mean free path. This is too short compared to the 1.4 Å C-C spacing for model of a simple metal.

In summary, heavily-doped $[CH]_x$ is not a simple metal as generally believed. There is no closed gap, uniform-bond state; instead, the bond length distortion of $[CH(ClO_4)_y]_x$ becomes uniformly incommensurate when $y > 0.045$. The signature of transition is a rise of the density of states at the Fermi surface (the gapless state induced by disorder) and a disappearance of $2\Delta_c$ interband transition.

APPENDIX

KRAMERS-KRONIG ANALYSIS

The Kramers-Kronig relation which relates the real part and imaginary part of a response function is based on causality. Causality means there can be no effect before the cause. According to reference 68, this relation can be derived by the following way.

If $G(t-t')$ is a response function which must satisfy the requirement of $G(t-t')=0$ for $t-t' < 0$, its fourier transform can be written as

$$G(\omega) = \int G(t-t')\exp[i\omega(t-t')]dt \tag{A-1}$$

If we let ω be complex, $\omega=\omega_1+\omega_2$ then Eq.A-1 becomes

$$G(\omega) = \int G(t-t')\exp[i\omega_1(t-t')]\exp[-\omega_2(t-t')]dt \tag{A-2}$$

From Cauchy's theorem

$$G(\omega) = \frac{1}{i\pi}\oint \frac{G(\omega')d\omega}{\omega' - \omega} \tag{A-3}$$

But in Eq.A-2, the factor $\exp[i\omega_1(t-t')]$ is bounded in the whole complex plane of ω; $\exp[-\omega_2(t-t')]$ is bounded only in upper half-plane for $t-t'>0$ and only in the lower half plane for $t-t'<0$. Since $G(t-t')=0$ for $t-t'<0$, $G(\omega)$ must be evaluated in the upper half-plane. So Eq.A-3 can be evaluated on the real axis of ω,

$$G(\omega) = \frac{1}{i\pi}\, P \int_{-\infty}^{\infty} \frac{G(\omega')d\omega'}{\omega' - \omega} \tag{A-4}$$

where P stands for principal value. If we split $G(\omega)$ into its real and imaginary parts, we get

$$\text{Re } G(\omega) = \frac{1}{\pi}\, P\int_{-\infty}^{\infty} \frac{\text{Im } G(\omega')}{\omega' - \omega}\, d\omega' \tag{A-5}$$

$$\text{Im } G(\omega) = -\frac{1}{\pi}\, P\int_{-\infty}^{\infty} \frac{\text{Re } G(\omega')}{\omega' - \omega}\, d\omega' \tag{A-6}$$

Eq.A-5 and Eq.A-6 is the socalled Kramers-kronig relation or dispersion relation which was derived by Kramers (1927) and Kronig (1926) independently.

The frequency dependent reflectance, $R(\omega)$, is a response function, since light cannot be reflected before the arrival of the incident light wave. $R(\omega)$ can be written as

$$R(\omega) = r(\omega)\ r^{*}(\omega) \qquad \text{(A-7)}$$

where $r(\omega)$ is the complex amplitude reflectivity which can be written as

$$r(\omega) = \rho(\omega)e^{i\theta(\omega)} \qquad \text{(A-8)}$$

then

$$R(\omega) = \rho^{2}(\omega) \qquad \text{(A-9)}$$

and

$$\ln\ [r(\omega)] = \ln\ [\rho(\omega)] + i\theta(\omega) \qquad \text{(A-10)}$$

According to Eq.A-5 and Eq.A-6,

$$\ln\ [\gamma(\omega)] = \frac{1}{\pi}\ P\int_{-\infty}^{\infty} \frac{(\omega')}{\omega' - \omega}\, d\omega' \qquad \text{(A-11)}$$

$$\theta(\omega) = \frac{1}{\pi}\ P\int_{-\infty}^{\infty} \frac{\ln\ [\rho(\omega')]}{\omega' - \omega}\, d\ \omega' \qquad \text{(A-12)}$$

Since the input and outpat function must be real, we require

$$r(-\omega) = r^{*}(\omega) \tag{A-13}$$

So Eq.A-12 can be rewritten as

$$\theta(\omega) = -\frac{2\omega}{\pi} P\int_{0}^{\infty} \frac{\ln \quad (\omega')}{(\omega')^{2} - \omega^{2}}\, d\omega' \tag{A-14}$$

Substituting $\rho(\omega) = R^{1/2}(\omega)$ into Eq.A-14, the phase angle $\theta(\omega)$ can be calculated by knowing the reflectance $R(\omega)$ for $\omega=0$ to $\omega=\infty$. In practice, the reflectance measurement only covers a limited frequency range. In order to evaluate Eq.A-14, we need to extrapolate the reflectance at both low and high frequency limit and do the integral numerically.

After calculated the phase angle $\theta(\omega)$, all of other important optical functions can be derived from it. By inverting the Fresnel relation:

$$r(\omega) = [n(\omega)-1 + ik(\omega)]/[n(\omega)+1 + ik(\omega)] \tag{A-14}$$

$n(\omega)$, the index of refraction; $k(\omega)$, the extinction coefficient can be derived. The absorption coefficient, $\alpha(\omega)$, is given by

$$\alpha(\omega) = (2\omega/c)k(\omega) \tag{A-15}$$

where c is the speed of light. The real and imaginary part of the complex dielectric function $\varepsilon_1(\omega)$ and $\varepsilon_2(\omega)$, related to n and k, is given by

$$\varepsilon_1(\omega) = n^2(\omega) - k^2(\omega) \tag{A-16}$$

$$\varepsilon_2(\omega) = 2n(\omega)k(\omega) \tag{A-17}$$

And the frequency dependent real conductivity, $\sigma_1(\omega)$, is

$$\sigma_1(\omega) = - \frac{\omega}{4\pi} \varepsilon_2(\omega) \tag{A-18}$$

REFERENCES

1. S. Etemad, A.J. Heeger and A.G. MacDiarmid, Annual Review of Physical Chemistry, 33, 443 (1982).

2. F.L. Carter, ed., Molecular Electronic Devices, Dekker, New York (1982).

3. A.R. Bishop, D.K. Campbell and K. Fesser, Mol. Cryst. Liq. Cryst., 77, 253 (1981).

4. J.R. Schrieffer, Mol. Cryst. Liq. Cryst., 118, 57 (1985).

5. T. Ito, H. Shirakawa and S. Ikada, J. Polymer Sci., Polymer Chem. Ed., 12, 11 (1974).

6. S.Roth, Physica, 127B, 151 (1984).

7. For recent advance, see Mol. Cryst. Liq. Cryst., 117 and 118 (1985).

8. S. Ikehata, J. Kaufer, T. Woerner, A. Pron, M.A. Druy, A. Sivak, A.J. Heeger and A.G. MacDiarmid, Phys. Rev. Lett., 45, 1123 (1980).

9. M.J. Rice, Physics Letters, 71A, 152 (1979).

10. W.P. Su, J.R. Shrieffer, and A.J. Heeger, Phys. Rev. Lett., 42, 1698 (1979); Phys. Rev., B22, 2099 (1980).

11. H.Takayami, Y.R. Lin liu, and K. Maki, Phys. Rev., B21, 2388 (1980).

12. S.Kivelson, Phys. Rev., B25, 3798 (1982).

13. A.J. Epstein, H.W. Gibson, P.M. Chaikin, W.G. Clark, and G. Gruner, Phys. Rev. Lett., 45, 1730 (1980).

14. S. Kivelson and A.J. Heeger, Phys. Rev. Lett., 55, 308 (1985).

15. J. Dong, Ph.D. dissertation, University of California, Santa Barbara, (1984).

16. C.K. Chiang, C.R. Fincher, Y.W. Park, A.J. Heeger, H. Shirakawa, E.J. Louis, S.C. Gau, and A.G. MacDiarmid, Phys. Rev. Lett., 39, 1098 (1977).

17. M.J. Rice, E.J. Mele, Chemica Scripta, 17, 121 (1981); E.J. Mele and M.J. Rice, Phys. Rev., B23, 5397 (1981).

18. T.W. Graham Solomons, Organic Chemistry, John Wiley and Sons, New York (1980).

19. R.E. Peierls, Quantum Theory of solid, Clarendon Press, Oxford, England (1955).

20. H. Frohlich, Proc. Roy. Soc., A223, 296 (1954).

21. A.R. Bishop, Solid State Communications, 33, 955 (1980)

22. J.A. Krumhansl and J.R. Schrieffer, Phys. Rev., B11, 3535 (1975).

23. P.G. de Gennes, Superconductivity of Metals and Alloys, Benjamin, New York, Chap. 5 (1966).

24. L.D. Landau and E.M. Lifshitz, Quantum Mechanics, Pergamon, New York, P72 (1958).

25. K. Fesser, A.R. Bishop, and D.K. Campbell, Phys. Rev., B27, 4804 (1983).

26. A.R. Bishop, D.K. Campbell and K. Fesser J. de Physique., 44-C3, 423 (1983).

27. D.K. Campbell and A.R. Bishop, Nuclear Physics, B200, 297 (1982).

28. R.F. Dashen, B. Hasslacher and A. NeVeu, Phys. Rev., D12, 2443 (1975).

29. P. Robin, J.P. Pouget, R. Comes, H.W. Gibson, and A.J. Epstein, Polymer, 24, 1558 (1983); J. de Physique (Paris) 44-C3, 87 (1983); Phys. Rev., B27, 3938 (1983).

30. E.A. Davis, N.F. Mott, Philos. Mag., 22, 903 (1970).

31. N.F. Mott, Philos. Mag., 19, 835 (1969).

32. I.G. Austin, N.F. Mott, Adv. Phys., 18, 41 (1969).

33. S. Kivelson and A.J. Epstein, Phys. Rev., B29, 3336 (1984).

34. J. Orenstein and G.L. Baker, Phys. Rev. Lett., 49, 1043 (1982).

35. S. Kivelson, Phys. Rev. Lett., 46, 1344 (1981).

36. A.J. Epstein, H. Rommelmann, R. Bigelow, H.W. Gibson, D.M. Hoffman, D.B. Tanner, Phys. Rev. Lett., 50, 1866 (1983).

37. T.C. Chung, F. Moraes, J.D. Flood, and A.J. Heeger, Phys. Rev., B29, 2341 (1984).

38. S. Kivelson, unpublished.

39. J. Chen, T.C. Chung, F.Moraes, and A.J. Heeger, Solid State Commun., 53, 757 (1985).

40. M.J. Rice, S. Strassler and W.R. Schneider Lect. Notes in Physics, 34, 282 (1975).

41. P.A. Lee, T.M. Rice and P.W. Anderson, Solid State Commun., 14, 703 (1974).

42. C.R. Fincher, M. Ozaki, A.J. Heeger, and A.G. MacDiarmid, Phys. Rev., B19, 4140 (1979).

43. E.J. Mele and M.J. Rice, Solid State Commun., 34, 339 (1980) Phys. Rev. Lett., 45, 926 (1980).

44. G. Herzberg, Infrared and Raman Spectra of Polyatomic Molecules. D. Van Nostrand Reihold, New York (1945).

45. J. Bart and C.H. MacGillvary, Acta Crystallogr. Sect., B24, 1569 (1968).

46. C.A. Coulson and H.C. Longuet Higgins, Proc. Roy. Soc., London, Ser. A193, 457 (1948).

47. R.G. Gavin and S.A. Rice, J. Chem. Phys., 55, 1675 (1971).

48. T. Kakitani, Prog. Theor. Phys., 51, 656 (1974).

49. H. Shirakawa, J. Ito, and S. Ikeda, Polym. J., 4, 460 (1973).

50. S.L. Hsu, A.J. Sinnorelli, G. Pez, and R. Baughman, J. Chem Phys., 69, 106 (1978).

51. S. Lefrant, L.S. Lichtman, H. Temkin, D.B. Fitchen, D.C. Miller, G.E. Whitewell, and J.M. Burlitch, Solid State Commun., 29, 1919 (1979).

52. M.J. Rice and E.J. Mele, Solid State Commun, 35, 487 (1980).

53. B. Horovitz, Phys Rev. Lett., 47, 1491 (1981).

54. B. Horovitz, Solid State Commun., 41, 593 (1982).

55. B. Horovitz, Solid State Commun., 41, 729 (1982).

56. S. Kivelson, Ting-Kuo Lee, Y.R. Lin-Liu, Ingo Peschel, and Lu Yu, Phys. Rev., B25, 4173 (1982).

57. N. Suzuki, M. Ozaki, S. Etemad, A.J. Heeger, and A.G. MacDiarmid, Phys. Rev. Lett., 45, 1209 (1980).

58. Karl Dieter Moller and Walter G. Rothschild, Far-Infrared Spectroscopy, John Wiley & Sons, Inc., New York (1971).

59. E.D. Palik and J.R. Stevenson, NRL Report, 6177 (1964).

60. R.J. Bell, Introductory Fourier Transform Spectroscopy, Academic Press, New York (1972).

61. S.I. Yaniger, M.J. Kletter, and A.G. MacDiarmid, Polym. Prepr., 25(2), 264 (1984).

62. A. Pron, Ph.D. Dissertation, University of Pennsylvania, (1980).

63. K. Soga, S. Kawakami, and H. Shirakawa, Macromol. Chem. Rapid Comm., 1, 643 (1980).

64. Y. Furukawa, T. Arakawa, H. Takeuchi, I. Harada, and H. Shirakawa, J. Chem. Phys., 81 2907 (1984).

65. A.J. Epstein, H. Rommelmenn, M. AbRowitz and H.W. Gibson, Polymer, 23, 88 (1982).

66. M. Abkowitz, P.G. Lecomber and W.E. Spear, Commun. on Physics, 1, 175 (1976).

67. F.G. Will, R.S. McDonald, R.D. Gleim, and M.R. Winkle, J. Chem. Phys., 78, 5847 (1983).

68. F. Wooten, Optical Properties of Solids, Academic Press, New York (1972).

69. D. Hoffman, Ph.D. Dissertation, Ohio State University, Columbus (1982).

70. J.L. Bredas, R. Sillbey, D.S. Boudreaux, and R.R. Chance, J. Am. Chem. Soc., 105, 6555 (1983).

71. E. Mulazzi, G.D. Brivio, E. Faulques, and S. Lefrant Solid State Commun., 46, 851 (1983).

72. A. Feldblum, J.H. Kaufmen, S. Etemad, and A.J. Heeger Phys. Rev., B26, 815 (1982).

73. A.J. Epstein, R.W. Bigelow, H. Rommelmenn, H.W. Gibson, R.J. Weagley, A. Feldblum, D.B. Tanner, J.P. Pouget, J.C. Pouxviel, R. Comes, P. Robin, and S. Kivelson, Mol. Cryst. Liq. Cryst., 117, 147 (1985).

74. M. Jestin, M. Kabbaj, J.P. Albert and C. Jouanin J. de Physique, 44, Colloq., C3-499 (1983).

75. T. Nogami, H. Mikawa and M. Nawa, J. de Physique, 44, Colloq., C3-573 (1983).

76. J. Tanaka, M. Tanaka, H. Fujimoto, K. Kamiya, Y. Saito and T. Kishi, Mol. Cryst. Liq. Cryst., 117, 259 (1985).

77. M.J. Rice, Phys. Rev. Lett. 37, 36 (1976); Z. Vardeny, E. Ehrenfreund, D. Brafman, and B. Horovitz, Phys. Rev. Lett., 51, 2326 (1983).

BIOGRAPHICAL SKETCH

Xiao-Qing Yang was born in Beijing, the People's Republic of China, on July 7th, 1949. He is the son of Ji-Zhi Yang and Yen Bai. He was raised in Beijing. His education was interrupted by the so-called "cultural revolution" when he was studying in the Fourth Secondary School of Beijing. He went to Shanxi Mechanical Engineering Institute to study physical metallurgy in 1973 and was awarded a B.S. in 1976. After working as an engineer in Tianjin Heavy Machinery Plant for about two years, he went to the Graduate School, Chinese Academy of Sciences to study physics. In 1981, he accepted an offer to enter the doctoral program in physics at Ohio State University, and spent one and a half years in Columbus, Ohio, working on his Ph.D. He followed his adviser, Dr. David Tanner, when he moved to the University of Florida in 1982, and has been engaged in research in the Department of Physics since then.

He is married to Lan-Feng Liu in 1977 and has a daughter, Bei Yang, who was born in 1978.

I certify that I have read this study and that in my opinion it conforms to acceptable standards of scholarly presentation and is fully adequate, in scope and quality, as a dissertation for the degree of Doctor of Philosophy.

David Tanner, Chairman
Professor of Physics

I certify that I have read this study and that in my opinion it conforms to acceptable standards of scholarly presentation and is fully adequate, in scope and quality, as a dissertation for the degree of Doctor of Philosophy.

Samuel Trickey
Professor of Physics

I certify that I have read this study and that in my opinion it conforms to acceptable standards of scholarly presentation and is fully adequate, in scope and quality, as a dissertation for the degree of Doctor of Philosophy.

Gary G. Ihas

Gary Ihas
Professor of Physics

I certify that I have read this study and that in my opinion it conforms to acceptable standards of scholarly presentation and is fully adequate, in scope and quality, as a dissertation for the degree of Doctor of Philosophy.

E. Dwight Adams

E. Dwight Adams
Professor of Physics

I certify that I have read this study and that in my opinion it conforms to acceptable standards of scholarly presentation and is fully adequate, in scope and quality, as a dissertation for the degree of Doctor of Philosophy.

Kenneth Wagener

Kenneth Wagener
Associate Professor of Chemistry

This dissertation was submitted to the Graduate Faculty of the Department of Physics in the College of Liberal Arts and Sciences and to the Graduate School and was accepted as partial fulfillment of the requirements for the degree of Doctor of Philosophy.

May 1986

Dean, Graduate School